

This article was downloaded by: [Dipartimento di Studi E Reicerche], [Raffaele Velotta]

On: 21 October 2011, At: 08:57

Publisher: Taylor & Francis

Informa Ltd Registered in England and Wales Registered Number: 1072954 Registered office: Mortimer House, 37-41 Mortimer Street, London W1T 3JH, UK



Journal of Modern Optics

Publication details, including instructions for authors and subscription information:

<http://www.tandfonline.com/loi/tmop20>

Single attosecond light pulses from multi-cycle laser sources

C. Altucci^a, J.W.G. Tisch^b & R. Velotta^a

^a CNISM and Dipartimento di Scienze Fisiche, University of Naples "Federico II", Via Cintia 26, Napoli, Italy

^b Blackett Laboratory, Imperial College London, Prince Consort Road, South Kensington, London SW7 2AZ, UK

Available online: 12 Oct 2011

To cite this article: C. Altucci, J.W.G. Tisch & R. Velotta (2011): Single attosecond light pulses from multi-cycle laser sources, *Journal of Modern Optics*, DOI:10.1080/09500340.2011.611913

To link to this article: <http://dx.doi.org/10.1080/09500340.2011.611913>



PLEASE SCROLL DOWN FOR ARTICLE

Full terms and conditions of use: <http://www.tandfonline.com/page/terms-and-conditions>

This article may be used for research, teaching, and private study purposes. Any substantial or systematic reproduction, redistribution, reselling, loan, sub-licensing, systematic supply, or distribution in any form to anyone is expressly forbidden.

The publisher does not give any warranty express or implied or make any representation that the contents will be complete or accurate or up to date. The accuracy of any instructions, formulae, and drug doses should be independently verified with primary sources. The publisher shall not be liable for any loss, actions, claims, proceedings, demand, or costs or damages whatsoever or howsoever caused arising directly or indirectly in connection with or arising out of the use of this material.

INVITED TOPICAL REVIEW

Single attosecond light pulses from multi-cycle laser sources

C. Altucci^{a*}, J.W.G. Tisch^b and R. Velotta^a

^aCNISM and Dipartimento di Scienze Fisiche, University of Naples “Federico II”, Via Cintia 26, Napoli, Italy;

^bBlackett Laboratory, Imperial College London, Prince Consort Road, South Kensington, London SW7 2AZ, UK

(Received 13 May 2011; final version received 28 July 2011)

High harmonic generation provides a means of producing attosecond pulses of light which are the shortest, controllable probes available to science for time-resolving ultrafast dynamics. We review techniques based on high harmonic generation for generating single attosecond pulses using high-power, multi-cycle laser sources, including optical-, polarisation-, and ionisation-gating schemes as well as techniques based on field synthesis. By significantly reducing the technical demands placed on the driving laser, these techniques have the potential to greatly broaden the application base for attosecond pulses.

Keywords: high harmonic generation; attosecond pulse; multi-cycle laser source

1. Introduction

High harmonic generation (HHG) is a remarkable frequency up-conversion process in which an ultrafast laser pulse (typically 5–100 fs) at high intensity ($>10^{14} \text{ W cm}^{-2}$) interacts with a gas-phase target to generate coherent extreme ultraviolet (XUV) radiation. HHG has been an intensively studied research topic for more than two decades [1–3].

In the last 10 years, it has emerged that, under the right conditions, HHG can produce XUV pulses of sub-femtosecond duration, i.e. of attosecond duration ($1 \text{ as} = 10^{-18} \text{ s}$) [4–6], providing scientists with the shortest controllable probes currently available for tracking ultrafast dynamics. Alongside this activity, it was discovered that the radiation emitted during HHG encodes structural information about the emitting molecule with sub-Ångstrom resolution as well as attosecond temporal resolution. Techniques to extract this information have come to be known as ‘HHG spectroscopy’ (for a review, see [7]). These two important developments have led to an explosion of research activity which has led to the creation of an exciting and vibrant research field known as ‘attosecond science’, which is already beginning to revolutionise our ability to observe and control electronic processes in matter [8]. Free electron lasers are sources capable of delivering femtosecond pulses with very high brilliance [9], thereby allowing the investigation of the non-linear behaviour of the matter exposed to high-intensity high-frequency laser field [10]. However, Attosecond Science currently relies on the XUV pulses produced through HHG, and HHG-based sources seem to provide the

most direct route to resolving electron dynamics down to the timescale of the atomic unit of time ($\approx 24 \text{ as}$).

One of the most important tools in the toolbox of attosecond science is the single attosecond pulse (SAP). As will be discussed in greater detail in following sections, attosecond light pulses can be generated by the HHG process in the form of attosecond pulse trains (ATPs), i.e. multiple attosecond pulses emitted each laser pulse (Figure 1(a)), or as SAPs, one isolated attosecond pulse emitted per laser pulse (Figure 1(b)). The generation of SAPs has largely been reliant on state-of-the-art laser sources capable of generating waveform-stabilised, high-intensity pulses of only a few optical cycles in duration.

The relatively recent development of techniques to produce SAPs with multi-cycle laser pulses (see Section 3), and often without the requirement of waveform stabilisation, has the potential to bring SAPs within the reach of a much wider scientific community. Furthermore, it seems likely that these techniques can be scaled to higher laser pulse energies. The resulting increase in the photon flux of the SAPs is expected to unlock a range of new experiments and scientific applications.

A number of general review articles have already been written on attosecond science [11–15]. The goal of this article, however, is to provide a timely review of the techniques for the generation of SAPs using multi-cycle laser pulses. We aim to provide a useful introduction to this important topic from the perspective of experimentalists working in the Attosecond Science field.

*Corresponding author. Email: altucci@na.infn.it

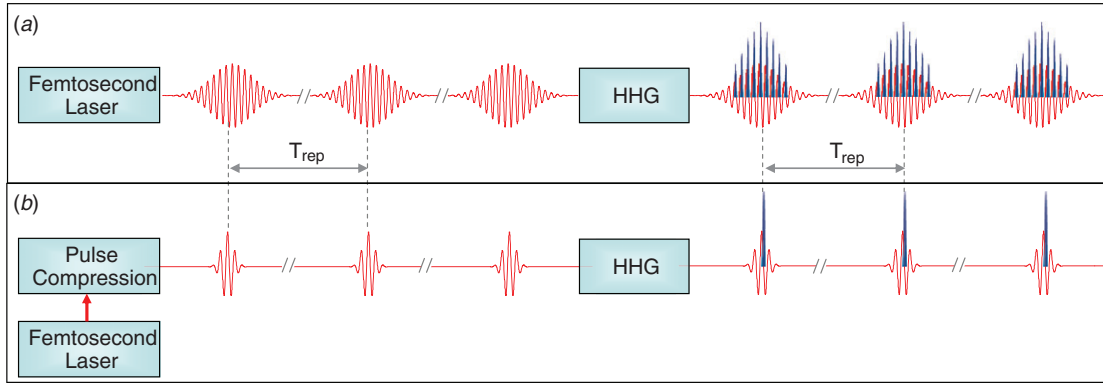


Figure 1. (a) Multi-cycle femtosecond laser pulses (electric field depicted by red line) driving the HHG process to produce attosecond pulse trains (intensity distribution shown in blue line). (b) Few-cycle, waveform stabilised laser pulses driving the HHG process to produce single attosecond pulse per laser pulse. $T_{\text{rep}} = 1/f_{\text{rep}}$ is the laser pulse spacing (typically $\sim 0.3\text{--}1$ ns), where f_{rep} is the pulse repetition rate of the laser. (The colour version of this figure is included in the online version of the journal.)

The review is organised as follows. Relevant background material is presented in Section 2, including an introduction to the process of HHG, a description of the main methods used to characterise SAPs, how SAPs are generated using few-cycle sources, and a summary of recent scientific applications of SAPs. Section 3 describes the generation of SAPs using multi-cycle laser pulses. It covers the techniques of polarisation gating (PG), double optical gating (DOG), generalised double optical gating (GDOG), and PG-like schemes that use multi-colour field synthesis and ionisation gating. While many of these techniques can be understood at the level of the single emitter of high harmonic radiation, propagation of the fields is now known to play an important role in the synthesis of stable SAPs and this is discussed in Section 4.

2. Background

2.1. High harmonic generation and attosecond pulses

HHG has been subject to a great deal of study. A variety of approaches have been adopted to model the process. Amongst these, the ‘three-step model’ (also known as the ‘recollision model’) [16,17] is particularly useful since it provides an intuitive description of the process. Though it is a semi-classical model, it reproduces the main qualitative features of HHG and provides insight into the formation of ATPs and SAPs. As illustrated in Figure 2, the three steps are: step 1, tunnel ionisation of the atom or molecule in the strong laser field with a probability that depends exponentially on the field strength; step 2, the acceleration of the resulting electron wavepacket in the continuum by the laser field with the electron treated classically and the Coulomb potential of the core neglected; and step 3, the radiative recombination of

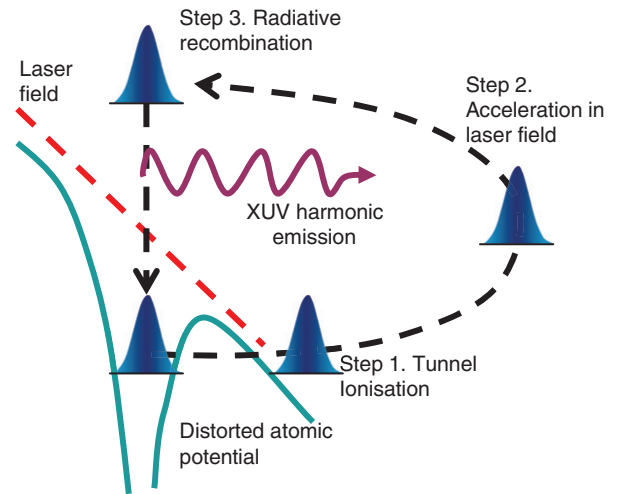


Figure 2. The three-step model of high harmonic generation. Note that the potential is not static during these steps. A snapshot of the potential is shown at the moment of ionisation. (The colour version of this figure is included in the online version of the journal.)

the electron wavepacket with the ion resulting in the emission of an XUV photon up to a maximum energy

$$E_{\text{max}} = I_p + 3.17U_p, \quad (1)$$

where I_p is the ionisation potential of the atom or molecule and

$$U_p = \frac{e^2 E_L^2}{4m_e \omega_L^2} \quad (2)$$

is the ponderomotive energy, which is the wiggles energy of a free electron of charge e and mass m_e in the laser electric field of field strength E_L and frequency ω_L .

For a laser pulse comprising a number of optical cycles each of sufficient field strength for tunnel

ionisation, these three steps are repeated a number of times with a periodicity of $T_L/2$, where $T_L = 2\pi/\omega_L$ is the laser period. The coherent superposition of the bursts of radiation arising from step 3 leads to an emission spectrum composed of discrete odd harmonics of the driving laser frequency, ω_L , as is readily understood from Fourier theory. For very short pulses (below about 3 cycles), the symmetry can be broken, leading to even order harmonics as well. The harmonics form a long plateau of roughly constant spectral intensity that ends in an abrupt cut-off at E_{\max} . In the time domain, the radiation emitted forms an APT with pulses separated by $T_L/2$, with one such train emitted per laser pulse [5,18] (see also Section 3). APTs with periodicity T_L have also been generated by two-colour driving fields ($\omega_L + 2\omega_L$) [19] where the presence of the second harmonic breaks the symmetry of the driving field so that only alternate half cycles are sufficiently strong for tunnel ionisation. This effect is also employed in optical gating schemes in which SAPs are generated with multi-cycle fields.

The classical electron trajectories correspond to quantum orbits in a Feynman Path Integral description of HHG [20]. For each harmonic order, two such quantum orbits contribute maximally to the emission. These are known as the ‘short’ and ‘long’ trajectories since they correspond to electron excursion times in the continuum of $\sim T_L/2$ and $\sim T_L$, respectively. Within the path integral description, the phase of the q th-order harmonic field relative to the laser field is given by

$$\phi_q = -\frac{S(\mathbf{p}, t, t')}{\hbar} + q\omega_L t, \quad (3)$$

where S is the semi-classical action given (in atomic units) by

$$S(\mathbf{p}, t, t') = \int_{t'}^t \left(\frac{1}{2} \mathbf{p} - \mathbf{A}(t'') \right)^2 + I_p \, dt'', \quad (4)$$

where t' and t are the time of ionisation and recombination, respectively, $\mathbf{p} = \mathbf{v} + \mathbf{A}(t)$ is the canonical momentum of the electron in a continuum state of kinetic energy $v^2/2$ and $\mathbf{A}(t)$ is the vector potential of the laser field.

An important result of the three-step model is that the classical electron trajectories exhibit dispersion in the recombination time. For example, an electron that is tunnel ionised close to the peak of the laser field spends more time in the continuum than one ionised at a later time. A full analysis shows that harmonic emission is to good approximation linearly chirped, with the short trajectory emission positively chirped and the long trajectory emission negatively chirped. In most experiments, the short trajectory emission is selected using propagation effects. Figure 3 shows experimental measurement of the positive linear chirp

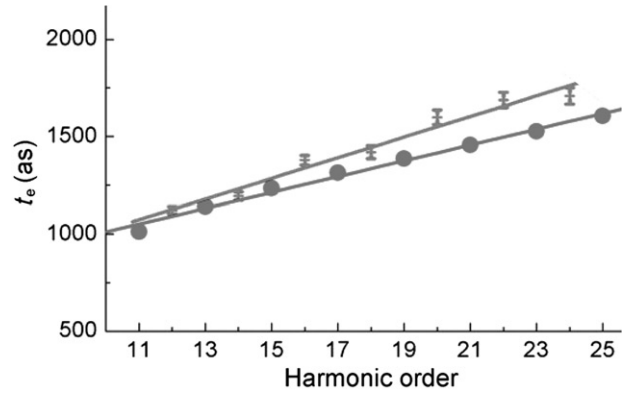


Figure 3. Harmonic emission time as a function of harmonic order (which is proportional to frequency) showing an approximately linear chirp on the emission. HHG was carried out in Ar at a laser intensity of $1.2 \times 10^{14} \text{ W/cm}^2$ with 50 fs laser pulses at 800 nm. Short trajectories were selected. The crosses are from two-photon, two-colour ionisation measurements. The points are single-atom predictions. Adapted with permission from Mairesse et al. [21]. Copyright (2003) by AAAS.

on the short trajectory emission [21]. This so-called ‘attochirp’ can be troublesome in the formation of SAPs and must be compensated to produce the shortest attosecond pulses [22]. However, it can also provide an accurate frequency to time mapping that allows, for example, molecular dynamics to be probed with attosecond temporal resolution through spectroscopic measurements [23,24].

The strong field approximation (SFA) model of HHG [25–27] is a widely-used quantum mechanical model that accounts for each step in the three-step model. It assumes (i) that the bound states of the atom are neglected apart from the ground state; and (ii) that the electron is driven as a free particle by the laser field in the continuum, with no influence from the atomic potential. Assumption (i) requires that resonant excitation by the fundamental wavelength can be neglected, which is true in most cases, especially when atoms are considered. Assumption (ii) relies on the consideration that the density of states in the continuum is high and the ionising oscillating wave packet spends most of its time outside the steepest part of the ionic potential.

Under these assumptions an analytic expression for the induced dipole moment can be obtained. It is given by (in atomic units)

$$x(t) = i \int_{-\infty}^t dt' \int d^3 \mathbf{p} E_L \cos(\omega_L t') d_x(\mathbf{p} - \mathbf{A}(t')) \times \exp(-iS(\mathbf{p}, t, t')) d_x^*(\mathbf{p} - \mathbf{A}(t)) + c.c. \quad (5)$$

where d_x is the component of the atomic dipole matrix element parallel to the laser polarisation,

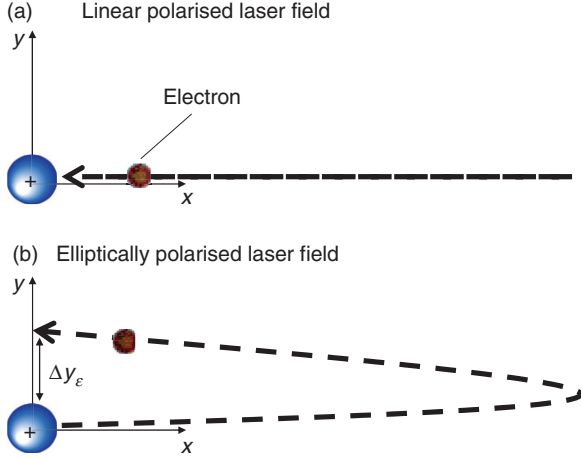


Figure 4. HHG for (a) a linearly polarised laser field, (b) an elliptically polarised laser field. (The colour version of this figure is included in the online version of the journal.)

$E_L \cos(\omega_L t') d_x(\mathbf{p} - \mathbf{A}(t'))$ give the probability for the electron to tunnel ionise to a continuum state with momentum \mathbf{p} at time t' (corresponding to step 1 in the three-step model); then acquiring a phase $\exp(-iS(\mathbf{p}, t, t'))$ as it propagate in the continuum between times t' and t (step 2); and then recombining with probability $d_x^*(\mathbf{p} - \mathbf{A}(t))$ at time t (step 3). The dipole moment can be Fourier decomposed to obtain the harmonic spectrum.

Of central importance to this review is the fact that HHG is sensitive to the polarisation state of the driving laser field. As illustrated in Figure 4(a), for a linearly polarised laser field, the electron wavepacket is driven along the polarisation axis of the laser and recollision with the ion core is ensured. However, in an elliptically polarised field the transverse field component ‘pushes’ the recolliding electron wavepacket to one side, as shown in Figure 4(b).

An elliptically polarised laser field can be written as $\mathbf{E}_L(t) = E_0 \cos(\omega t) \mathbf{x} + \varepsilon E_0 \sin(\omega t) \mathbf{y}$, where ε is the ellipticity, with $\varepsilon = 0$ corresponding to linear polarisation along \mathbf{x} , while $\varepsilon = 1$ corresponding to circular polarisation. For the case $\varepsilon \ll 1$ where the dominant electron motion is along \mathbf{x} , the electric field component along \mathbf{y} displaces the maximum energy recolliding electrons close to $(3.17U_p)$ by an amount [28] given by

$$\Delta y_\varepsilon \approx \frac{5\varepsilon e E_0}{m_e \omega_L^2}. \quad (6)$$

This displacement reduces the overlap of the recolliding electron wavepacket with the core, thus reducing the HHG amplitude. When Δy_ε exceeds the spatial width of the wavepacket along \mathbf{y} , HHG is effectively terminated. Under typical conditions for HHG the recolliding wavepacket has spread to $\sim 10 \text{ \AA}$ when it

returns to the vicinity of the core [29]. According to Equation (6), for a typical peak laser intensity of $I_0 = 10^{14} \text{ W cm}^{-2}$ and $\lambda_L = 800 \text{ nm}$, an ellipticity of $\varepsilon \approx 0.2$ is thus sufficient for the wavepacket to ‘miss the core’. This estimate is broadly in agreement with experimental measurements that show that the HHG emission is reduced by about a factor of ten for $\varepsilon \approx 0.2$ compared to linear polarisation [15,27,30]. This strong ellipticity dependence of HHG is harnessed usefully in polarisation gating schemes (described in Section 3), where a time-varying ellipticity is introduced on the laser pulse which acts to temporally confine the high harmonic emission to a narrow ‘gate’ of near linear polarisation, as shown in Figure 5.

APTs have pulse repetition rates typically in the petahertz range ($f_{\text{rep}} = 2/T_L$ or $f_{\text{rep}} = 1/T_L$ for symmetry breaking schemes). For general time-resolved measurements, SAPs are extremely useful since they provide one isolated attosecond pulse per laser pulse and are thus well-suited to general pump-probe schemes. Initially, polarisation gating schemes were proposed to achieve SAPs via HHG [32] though progress came first through a temporal confinement of the HHG process brought about by reducing the drive laser pulse duration to the few-cycle limit [6,33]. In this limit, where the laser pulse duration, τ_L , becomes comparable to T_L , the amplitude of consecutive half-cycle laser field oscillations can vary significantly. One half-cycle can be appreciably stronger than all others in the pulse. As illustrated in Figure 6, the electron wavepacket recollision energy from this half-cycle is correspondingly higher and so the radiation emitted from this recollision – constituting a continuum in the cutoff region of the HHG spectrum – can be isolated by a bandpass spectral filter, for example by passing the radiation through a thin foil or using the reflectance bandwidth of a multilayer XUV mirror. Foil filters (e.g. Al) have the additional advantage that their material dispersion can compensate the attochirp of the pulse leading to a shorter SAP [22].

An effect that becomes significant in the few-cycle limit is the sensitivity of the electric-field waveform to the carrier-envelope phase (CEP) [34]. The CEP is the phase offset between the peak of the pulse envelope and the nearest peak of the carrier wave. Writing the electric field of a laser pulse as

$$E_L(t) = E_0(t) \cos(\omega_L t + \phi), \quad (7)$$

where $E_0(t)$ is the pulse envelope, the CEP is given by ϕ . A field-driven process such as HHG is particularly sensitive to the CEP in the few cycle limit [34]. Figure 7 shows the results of a Quantum Orbits simulation of HHG [35] for the HHG signal produced within a realistic bandpass spectral filter for four different

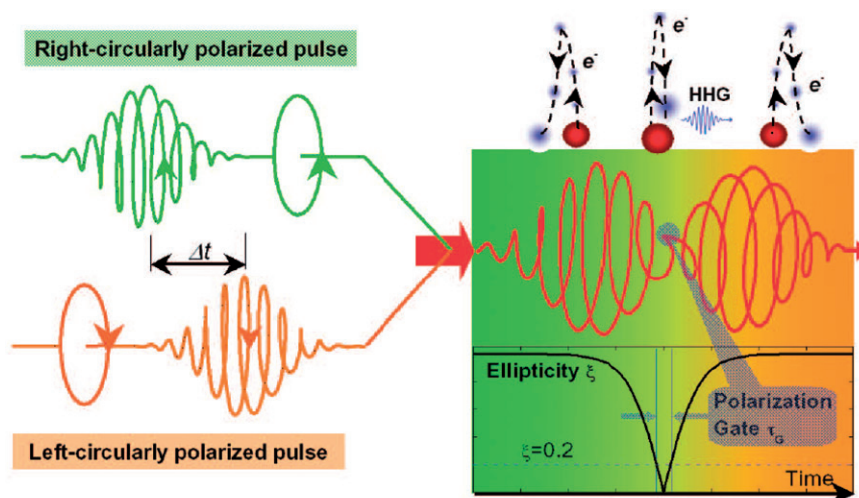


Figure 5. A pulse with a time-dependent ellipticity, $\varepsilon(t)$, can be synthesised from time-delayed left and right-hand circularly polarised laser pulses. Re-collision occurs during a narrow ‘polarisation gate’ at the pulse centre where ε is close to zero. Reproduced with permission from Shan et al. [31]. Copyright (2005) by Taylor & Francis. (The colour version of this figure is included in the online version of the journal.)

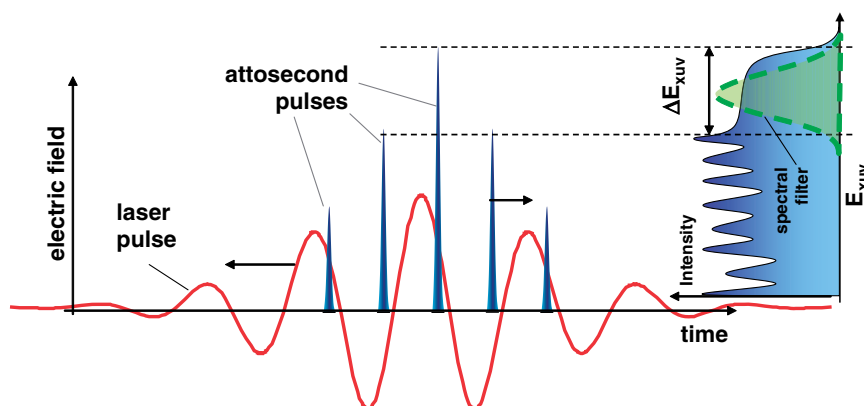


Figure 6. SAP generation in the few-cycle laser pulse regime can be achieved by band-pass spectral filtering of the continuum radiation at the cut-off of the HHG spectrum. E_{xuv} is the XUV photon energy and ΔE_{xuv} is the bandwidth of the continuum. Note that the height of the attosecond pulses is proportional to their photon energy (right-hand axis). (The colour version of this figure is included in the online version of the journal.)

values of the CEP, ϕ (see caption for details). The optimal value of ϕ in terms of maximum attosecond pulse intensity and highest contrast relative to satellite pulses is $\phi \approx \pi/2$, which was found to depend on the peak laser intensity and pulse duration.

In the HHG process, each consecutive half-cycle of the laser pulse produces harmonic emission with a characteristic photon energy cutoff that is related to the instantaneous intensity of the drive pulse [36,37]. Each of these so-called ‘half-cycle cut-offs’ (HCOs) – if isolated from plateau emission and other HCOs – can constitute a SAP. As shown in Figure 6, usually the highest energy HCO is selected for SAP generation, since its higher energy spectrum is distinct from lower energy HCOs. However, in [35] it was shown

experimentally that under the right phase-matching conditions the HCOs become spatially separated and can be isolated using spatial filtering. Furthermore, it was demonstrated in [35] that the energies of the HCOs can be tuned by varying the CEP of the drive pulse.

So far our description of HHG and the generation of ATPs and SAPs has been a single-emitter picture (atom or molecule). Under normal experimental conditions, it is in fact the coherent superposition of the radiation from a very large number, N , of emitters (typically $N \sim 10^{12}$) that is responsible for the measured HHG signal. The nature of this superposition is a relatively complex problem known as ‘phase-matching’ that depends on the spatial and temporal variation of the emitter density and propagation of the laser field

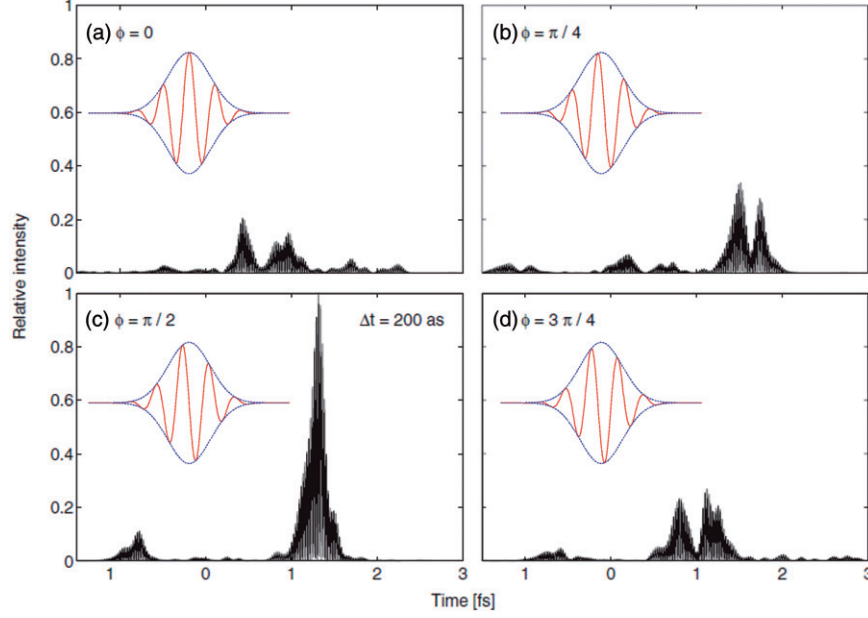


Figure 7. Numerical simulations of XUV pulses from HHG (black filled curved) showing the sensitivity of SAP generation to the CEP. The simulations were for HHG in Ne at $5 \times 10^{14} \text{ W/cm}^2$ driven by a 5 fs laser pulse of centre wavelength 750 nm. A Gaussian spectral bandpass filter of width 9 eV centred at 92 eV was used. For these conditions, the optimal CEP for SAP generation is $\phi \approx \pi/2$. The insets show the laser electric field waveforms for the different CEP values. Adapted from Chipperfield et al. [35]. (The colour version of this figure is included in the online version of the journal.)

within the interaction volume [38,39]. Due to a mismatch between the phase velocities of the laser and harmonic waves in the general case, the length in the medium over which constructive interference occurs for the q th order harmonic is limited to a distance known as the coherence length, $L_q^{(\text{coh})} = \pi/\Delta k_q$ where $\Delta k_q = k_q - qk_L$ is the phase-mismatch, and k_L and k_q are the wave vectors of the laser and harmonic fields, respectively. For maximum HHG efficiency, the goal is to minimise the phase-mismatch. In HHG, there are a number of contributions to Δk_q

$$\Delta k_q^{(\text{HHG})} = \Delta k_q^{(\text{neutral gas})} + \Delta k_q^{(\text{free electrons})} + \Delta k_q^{(\text{geometric})} + \Delta k_q^{(\text{dipole})}, \quad (8)$$

where $\Delta k_q^{(\text{neutral gas})}$ is the contribution arising from the dispersion of the neutral generating medium (which is usually negative); $\Delta k_q^{(\text{free electrons})} \propto n_e q \lambda_L$ is the positive contribution from the dispersion of free electrons (density n_e) produced from laser-induced ionisation of the medium; $\Delta k_q^{(\text{geometric})}$ is a positive geometric contribution that arises from the Gouy phase shift ($\propto q/b$ on axis for loose focusing, where b is the laser confocal parameter) as the laser passes through its focus, or arising from waveguide dispersion ($\propto \lambda_L/a^2$) in cases where HHG is carried out in a hollow capillary (inner radius a) that guides the laser beam [40], and $\Delta k_q^{(\text{dipole})} \propto -I_0 z/b^2$ (again on axis, for loose focusing), where I_0 is

the peak laser intensity and z the propagation axis, is a contribution which changes sign before and after the laser focus that comes from the intrinsic intensity-dependent phase of the harmonic dipole (Equation (3)).

In general, all of these contributions can be minimised through a combination of using a relatively low gas density for the generating medium, employing laser intensities below the ionisation saturation intensity for the medium, and using loose laser focusing (such that $b \gg L$, where L is the length of the generating medium), while still maintaining an intensity above $\sim 10^{14} \text{ W cm}^{-2}$. Component phase mismatches of different sign can also be balanced against each other to minimise $\Delta k_q^{(\text{HHG})}$ [42]. Under carefully optimised phase-matching conditions, HHG beams can exhibit very high beam quality [43,44] and near perfect transverse spatial coherence [45,46], which means that APT and SAP sources can, in principle, have the spatial and coherence properties of high quality laser beams.

The phase-matching conditions also provide a means for the experimentalist to select quantum trajectories associated with the single emitter response [20]. For example, short trajectories can be isolated by ensuring the driving laser is focused slightly before the generating medium and using an on-axis aperture downstream of the interaction volume to pass the lower divergence HHG emission.

2.2. Characterising SAPs

'Attosecond streaking' is the most widely used technique for the temporal characterisation of SAPs [33,47,48]. The basic principle of attosecond streaking (illustrated in Figure 8) can be likened to an atomic version of the electro-optical streak camera [49]. An electron pulse is first created by photoionisation of a gas target by the XUV SAP. This electron pulse is assumed to be a temporal replica of the SAP. The electrons are then 'streaked' (i.e. they pick up momentum) from the electric field of the driving laser pulse. This results in a shift of their kinetic energy that depends of the value of the laser vector potential at the moment of ionisation. By streaking with the laser field of the pulse used to generate the SAP, this technique takes advantage of the intrinsic attosecond synchronisation between the SAP and the laser field.

From a semi-classical analysis [33], the final streaked electron kinetic energy W_f is given by

$$W_f \approx W_0 - U_p(\tau) + U_p(\tau) \cos(2\omega_L \tau) + 4U_p(\tau) \cos^2 \theta \sin^2(\omega_L \tau) + \sqrt{8W_0 U_p(\tau)} \cos \theta \sin(\omega_L \tau), \quad (9)$$

where $W_0 = \hbar\omega_{\text{SAP}} - I_p$ is the initial energy of the photoelectrons following photoionisation by a XUV SAP of frequency ω_{SAP} , τ is the delay time between the SAP and the laser pulse,

$$U_p(t) = \frac{e^2 E_L^2}{4m_e \omega_L^2},$$

and θ is the detection angle with respect to the laser polarisation.

In a streaking measurement, the SAP and the driving laser field are focused into a gas target and the photoelectron energies are typically measured using a time-of-flight spectrometer. Their energy spectra are recorded as a function of delay, τ , over a range of several laser half-cycles. The delay between the SAP and driving pulse is scanned using a piezo-actuated split mirror [33] or a Mach-Zender interferometer [50,51]. Due to low photoelectron count rates, a complete delay scan requires a large number of laser shots (usually $\geq 10^6$) which even at 1 kHz laser pulse repetition rates necessitates scan times of order ~ 0.5 h, during which time CEP stabilisation must be maintained.

For photoelectron detection along the laser polarisation axis ($\theta=0^\circ$) the intensity distribution of the SAP is mapped onto the streaked photoelectron distribution, allowing the SAP profile to be determined. Figure 9(a) shows streaking data with $\theta=0^\circ$ obtained using 5 fs, 750 nm CEP stabilised laser pulses to streak photoelectrons produced in Ar by SAPs

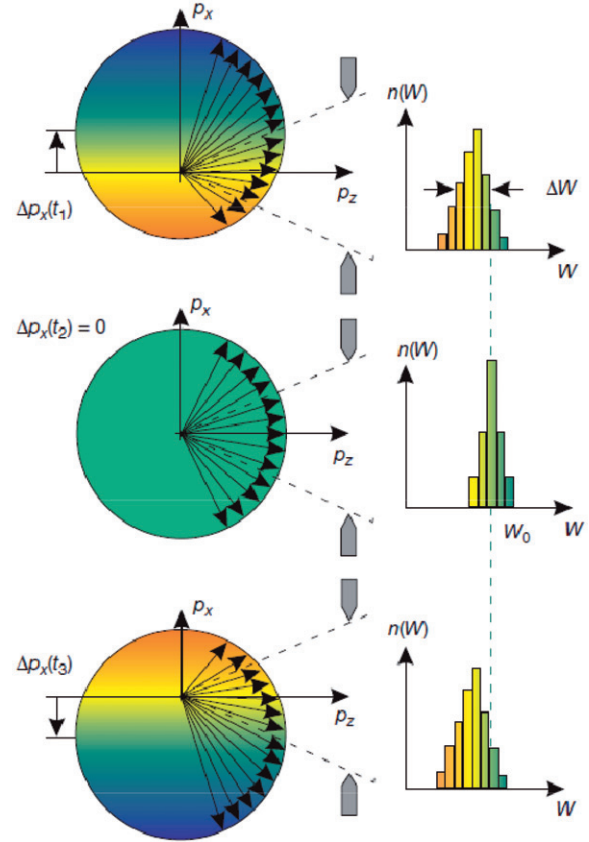


Figure 8. The basic principle of attosecond streaking. Atoms are single-photon ionised by the XUV SAP in the presence of the time-delayed laser electric field. The initially isotropic photoelectron momentum distribution is 'shifted' by the laser field leading to a modification of the detected kinetic energy (W) spectrum (illustrated as histograms). Here Δp is the field induced momentum change and t_1 , t_2 and t_3 are three delay values corresponding to the peak of the SAP coinciding with a zero crossing (maximum positive momentum shift), a maximum (zero momentum shift), and zero crossing of opposite slope (maximum negative momentum shift) of the laser electric field, respectively. The laser polarisation is in the x direction and the detection axis is perpendicular to this along z . Reproduced with permission from Hentschel et al. [6]. Copyright (2001) by Nature Publishing Group. (The colour version of this figure is included in the online version of the journal.)

at 36 eV. The SAPs were generated via HHG in Ar using polarisation gating [51]. Streaking at $\theta=90^\circ$ is also possible [33]. In this geometry, the last two terms in Equation (9) vanish. Without the last term, the streaking amplitude, $W_f - W_0$, is independent of the initial photoelectron energy, W_0 . This is beneficial for characterising very short SAPs whose broad bandwidth leads to a significant spread in the initial photoelectron energy.

Though initially used to obtain just the temporal intensity distribution of the SAP, streaking data, such as Figure 9(a), can contain sufficient information to

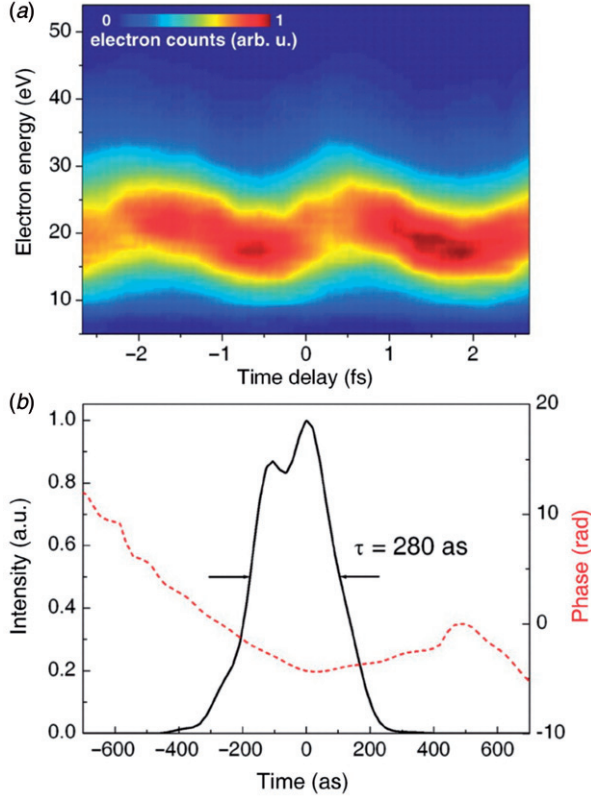


Figure 9. SAP generation in Ar using polarisation gating. (a) Streaking data; (b) SAP reconstruction using the FROG-CRAB technique. The solid line is the pulse intensity, the dashed line is the temporal phase. Reproduced with permission from Sansone et al. [51]. Copyright (2006) by AAAS. (The colour version of this figure is included in the online version of the journal.)

allow a complete reconstruction of the SAP electric field. This is because the streaking field acts as an attosecond phase modulator on the electron wavepacket. The two-dimensional streaking data (photoelectron data versus delay) thus can be treated as a spectrogram, given by [48]

$$s(\omega, \tau) = \left| \int_{-\infty}^{\infty} G(t) E_{\text{SAP}}(t - \tau) e^{i\omega t} dt \right|^2, \quad (10)$$

where $E_{\text{SAP}}(t)$ is the electric field of the SAP to be characterised and $G(t)$ is a ‘phase-gate’ given by $G(t) = \exp[i\Phi(t)]$. Within the SFA framework, the phase modulation is given by [48]

$$\begin{aligned} \Phi(t) = & - \int_t^{\infty} U_p(t') dt' - \frac{U_p(t)}{2\omega_L} \sin(2\omega_L t) \\ & + \frac{\sqrt{8W_0 U_p(t)}}{\omega_L} \cos \theta \cos(\omega_L t). \end{aligned} \quad (11)$$

It is possible to extract the phase and amplitude of the SAP field by applying frequency resolved optical gating (FROG [52]) retrieval algorithms [53] to the

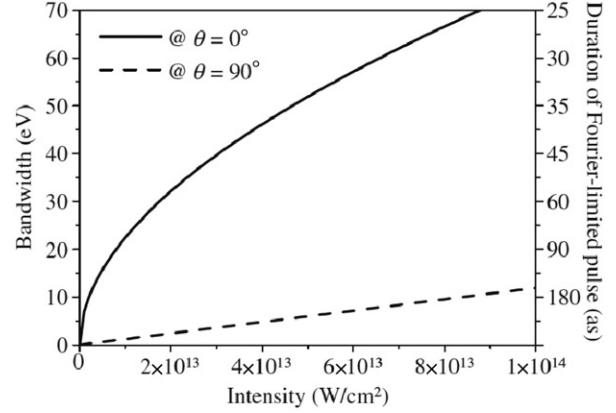


Figure 10. Calculated energy bandwidth (left axis) of the FROG-CRAB technique as a function of streaking intensity for electron detection parallel ($\theta=0^\circ$) and perpendicular ($\theta=90^\circ$) to the laser polarisation. The minimum SAP duration that could be characterised ($\sim 1/\text{bandwidth}$) is shown on the right axis. The calculations are for a 100 eV SAP and a 800 nm streaking field. Reproduced with permission from Quéré et al. [54]. Copyright (2005) by Taylor & Francis.

spectrogram $s(\omega, \tau)$. This characterisation technique is known as FROG-CRAB [48,54], where CRAB stands for complete reconstruction of attosecond bursts.

Figure 9(b) shows the intensity profile and the temporal phase of a SAP that was reconstructed using the FROG-CRAB technique from the streaking data in (a) of this figure. The use of FROG-CRAB to measure the SAP phase enables phase distortions to be corrected and the SAP duration to be reduced towards the transform limit. The observed quadratic temporal phase (linear chirp) seen in Figure 9(b) is due to the attochirp. In the same experiment this was compensated for by passing the SAP through a 300 nm thick Al foil. The resulting temporal phase of the SAP became almost flat and the pulse duration was reduced by more than a factor of two to 130 as.

The bandwidth, $|\partial\Phi/\partial t|_{\text{max}}$, of the electron phase modulation provided by streaking increases with the intensity of the streaking field and is significantly greater for the $\theta=0^\circ$ geometry, as shown in Figure 10 for a 100 eV SAP and a 800 nm streaking field [54]. The temporal resolution of FROG-CRAB ($\sim 1/\text{bandwidth}$) is seen to be < 50 as for a streaking field intensity of more than $\sim 2 \times 10^{13} \text{ W cm}^{-2}$ for the $\theta=0^\circ$ case, but it is worth noting that high streaking fields can lead to unwanted ionisation.

2.3. SAPs generated by few-cycle lasers

To achieve peak laser intensities of greater than $\sim 10^{14} \text{ W cm}^{-2}$ required for HHG using femtosecond

pulses (given the requirement for relatively loose focusing) typically demands millijoule level laser pulses. For pulse durations greater than ~ 25 fs, these can be obtained from commercially-available Ti:sapphire chirped pulse amplification lasers that operate in the near infrared (NIR) at $\lambda_L \approx 800$ nm (for a review, see [55]). To produce high-power pulses in the few-cycle limit (less than ~ 6 fs at 800 nm) requires external ‘‘pulse compression’’ techniques to be applied to reduce the pulse duration by a factor greater than ~ 5 . Since the laser pulses direct from the laser are typically close to transform limited, the standard way of achieving this is by spectrally broadening the pulse by a factor greater than ~ 5 in a gas-filled hollow fibre [56–59] followed by pulse compression using dielectric chirped mirrors [60]. The chirped mirrors compensate the chirp on the pulse, allowing near transform limited pulses to be attained, now more than ~ 5 times shorter than the original laser pulse. State-of-the-art parameters for hollow fibre pulse compression are pulse durations below 4 fs [61–63] and pulse energies up to 5 mJ [64].

Though optical gating schemes (see Section 3) can relax the requirements for waveform stabilisation, in general CEP stabilisation is necessary for stable SAP generation and represents an important enabling technology for attosecond science. CEP-stabilisation is achieved by employing ‘f–2f’ interferometry [65] to measure the CEP drift of the laser pulses and using feedback to the laser to stabilise the CEP [66,67].

The very short pulse durations available from hollow fibre pulse compression (~ 1.5 cycles) are very effective in isolating a SAP in the HHG process. Analysis of classical electron trajectories indicates that the minimum SAP duration attainable using spectral selection of the HHG cutoff continuum is given by [41]

$$\Delta t_{\text{SAP}}^{(\text{min})} \approx 3000 N_c^2 / E_{\text{SAP}} \quad (12)$$

where $\Delta t_{\text{SAP}}^{(\text{min})}$ is in attoseconds, E_{SAP} is the photon energy of the SAP in electron-volts and N_c is the number of optical cycles in the full width at half maximum of the laser pulse. Note that this transform limited pulse duration can only be reached if any chirp on the SAP, including the attochirp can be fully compensated. In [68], CEP stabilised, ~ 3.3 fs laser pulses ($\lambda_L = 720$ nm) were used to drive HHG in Ne. SAPs of 80 as centred at ~ 80 eV were measured using FROG-CRAB (see Figure 11), which is the shortest SAP so far reported. For $N_c = 1.5$ and $E_{\text{sap}} = 80$ eV, Equation (12) gives $\Delta t_{\text{SAP}}^{(\text{min})} \approx 84$ fs, in good agreement with the measured pulse duration. In this experiment, a Zr foil filter was used for attochirp compensation. Since N_c has a minimum value of ≈ 1 , Equation (12) tells us that SAP generation from spectral filtering of

the cutoff will only yield pulses significantly below 80 as by using higher photon energies.

Ionisation and phase-matching effects that occur during the HHG process have been used to enhance SAP generation. Ionisation of the generating medium on the rising edge of the laser pulse leads to an electron density $n_e(t)$ that increases rapidly and monotonically in time during the pulse. As $n_e(t)$ increases, $\Delta k_q^{(\text{HHG})}(t)$ can sweep through a minimum as the positive contributions to the phase-mismatch from the free electrons transiently offset negative phase-mismatch contributions. Since the HHG intensity is proportional to $\text{sinc}^2(\Delta k_q^{(\text{HHG})}(t)L/2)$, where L is the length of the generating medium, this effect can provide a temporally narrow gate of enhanced phase-matching. Through careful choice of phase-matching parameters, this ‘phase-matching gate’ has been shown to be able to isolate a SAP even for somewhat longer laser pulses than used typically for SAP generation in the few-cycle regime. In [69], a 430 as SAP was generated using 8 fs laser pulses (~ 3 cycles). In [70], SAP generation was reported using 15 fs pulses (~ 6 cycles) to drive HHG in a capillary waveguide.

Ionisation on the rising edge of the pulse can also deplete the ground state population of the generating medium if the peak laser intensity exceeds the ionisation saturation intensity, I_{sat} , of the medium. Once the ground state population is depleted HHG is terminated. This provides an ‘ionisation gate’ which opens when the instantaneous laser intensity is sufficiently high for tunnel ionisation (and hence HHG) and closes when the ground state becomes depleted. Provided the pulse is sufficiently short to begin with, this can be used to isolate a SAP, as discussed theoretically in [71,72].

Recently ionisation gating above I_{sat} has been demonstrated experimentally using 5 fs, CEP stabilised laser pulses of peak intensity $2.3 \times 10^{15} \text{ W cm}^{-2}$ to drive HHG in Xe [73]. This intensity is $\sim 17 \times$ higher than I_{sat} for Xe at this pulse duration. For the correct CEP value, the ionisation gate under these conditions is sufficiently narrow that the entire HHG spectrum was observed to become continuous (including plateau region). Similar behaviour was reported for Kr, Ar and Ne [73]. In Xe, a ~ 160 as SAP centred at 30 eV was measured using FROG-CRAB. Since spectral filtering was not required to isolate a cutoff XUV continuum, the SAP energy was ~ 2 nJ/pulse ($\sim 5 \times 10^8$ photons/pulse) which is more than two orders of magnitude higher than previous SAP pulse energies at a similar photon energy [74]. The authors of [73] point out that if such a SAP could be focused to a $\sim 2.5 \mu\text{m}$ spot, a peak intensity of $\sim 7 \times 10^{13} \text{ W cm}^{-2}$ could be achieved, well above the threshold for two photon transitions in

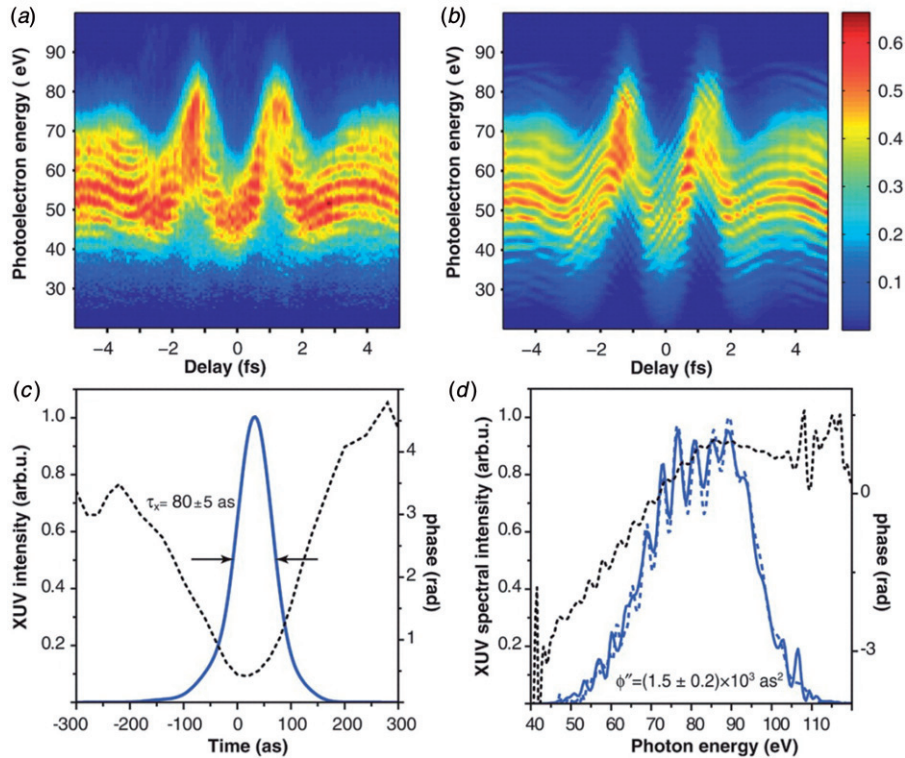


Figure 11. 80 as SAP generation from HHG in Ne using 1.5 cycle NIR laser pulses. (a) Streaking data; (b) FROG-CRAB reconstruction; (c) retrieved SAP intensity profile (solid line) and temporal phase (dotted line); (d) retrieved SAP spectrum (solid line) and spectral phase; note residual positive chirp. Reproduced with permission from Goulielmakis et al. [68]. Copyright (2007) by AAAS. (The colour version of this figure is included in the online version of the journal.)

the XUV. This seems to open the door for attosecond nonlinear optics.

In Ne a continuous HHG spectrum extending from 65–160 eV was observed [73], which has sufficient bandwidth to support a SAP of duration ~ 20 as. We note that the ionisation gating technique appears to allow much shorter SAPs than the limit imposed by Equation (12). However, chirp compensation over such a broad spectrum is likely to represent a formidable challenge.

2.4. Applications of SAPs

The early research in attosecond science was heavily focused on developing the technology and techniques for the generation and characterisation of APTs and SAPs. This pioneering work developed the tools of attosecond science and has laid the foundation for recent experiments in which attosecond pulses are being used to measure ultrafast dynamics in matter on an unprecedented timescale. In fact, attosecond streaking that was originally developed for characterising SAPs has proved to be an important technique for making attosecond-resolution measurements. In this

section, we briefly review some recent experimental applications of SAPs.

The first application of a SAP was a time-domain measurement (Figure 12) of the lifetime of an inner-shell electron vacancy in Kr using attosecond streaking [75]. The short lifetime of the vacancies under study (few fs) mandated the use of an XUV pulse of sub-fs duration to produce the hole. In this experiment, a ~ 100 eV, 900 as duration SAP was used. The resulting Auger electrons were streaked by a time-delayed 7 fs, 750 nm NIR pulse allowing the lifetime of the $M(d5/2)$ vacancy to be measured. A lifetime of ~ 8 fs was obtained, in good agreement with an earlier energy-domain measurement [76]. In [75] the authors point out that time-domain measurements of inner-shell electron dynamics using SAPs are advantageous for systems in which the interference of multiple relaxation pathways make an energy-domain analysis problematic.

SAPs of ~ 250 as duration and photon energy of ~ 90 eV were used to make the first real-time observation of light-induced electron tunnelling in an atom [77]. In this pump-probe experiment, the XUV SAP created Ne^+ ions with electrons in excited, so-called ‘shake-up’ states. These were then preferentially tunnel ionised by a CEP-stabilised, time-delayed 5.5 fs NIR

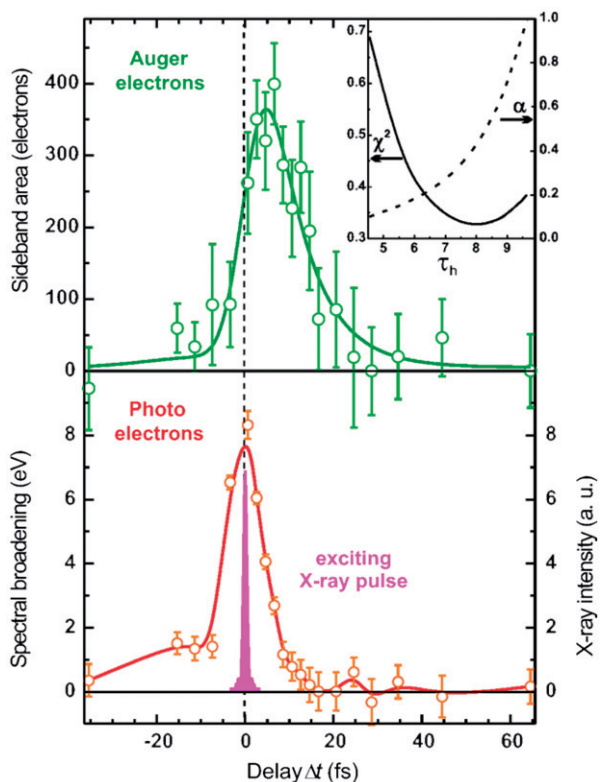


Figure 12. The first time-domain measurement of inner shell electron dynamics using attosecond streaking. (a) The Auger electron signal in Kr (corresponding to the lowest energy $M_{4,5}N_1N_{2,3}$ Auger line) as a function of delay with respect to NIR streaking pulse. Fitting an exponential decay curve allows the lifetime of the M-shell vacancy to be determined. (b) Spectral broadening of the $4p$ photo-line recorded at the same time from which information about the sampling function required for the deconvolution was obtained. Reproduced with permission from Drescher et al. [75]. Copyright (2009) by Nature Publishing Group. (The colour version of this figure is included in the online version of the journal.)

pulse at an intensity of $\sim 7 \times 10^{13} \text{ W cm}^{-2}$. The Ne^{2+} yield as a function of delay was found to increase in a series of steps spaced by $T_L/2$, thus following the field oscillations of the NIR pulse. This observed behaviour is consistent with field-induced tunnelling of the Ne^+ shake-up states.

As well as the gas-phase experiments described above, SAPs have also been applied to the study of ultrafast physics in condensed-matter systems and on surfaces. SAPs of 300 as duration and photon energy $\sim 91 \text{ eV}$ together with time-delayed CEP stabilised 5fs, 750 NIR pulses were used in an attosecond streaking experiment to time-resolve the electron-transport step in photoelectron emission from single-crystal tungsten [78]. As can be seen in Figure 13, a delay of $110 \pm 70 \text{ as}$ was measured between photoelectrons from localised $4f$ states of the metal and those from delocalised

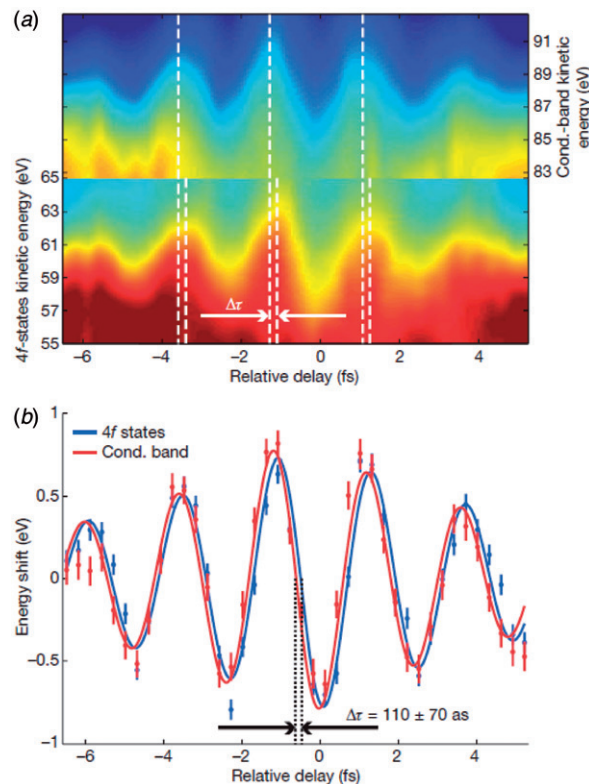


Figure 13. Attosecond streaking data that measures a delay of $110 \pm 70 \text{ as}$ between the emission of $4f$ and conduction band electrons from a single-crystal tungsten surface by a 300 as SAP. (a) The streaking spectrogram; (b) the energy shifts of the $4f$ (blue curve) and conduction-band (red curve) electrons obtained by considering electron kinetic energies in the spectrogram in the intervals 47–66 eV and 66–110 eV, respectively. Reproduced with permission from Cavalieri et al. [78]. Copyright (2007) by Nature Publishing Group. (The colour version of this figure is included in the online version of the journal.)

conduction-band states, with the delocalised photoelectrons appearing first. The authors attributed this delay to a higher mean velocity ($\times 2$) of the conduction-band electrons and the fact that the ‘slower’ $4f$ electrons originated from $\sim 1 \text{ \AA}$ deeper in the metal surface.

A similar type of experiment also using attosecond streaking was conducted in gas-phase Ne atoms to measure the delay between the photoemission of electrons from $2s$ and $2p$ states following the absorption of a SAP of $< 200 \text{ as}$ duration and 106 eV photon energy [79]. In the non-resonant case, the delay would be typically presumed to be close to zero. However, a delay of $21 \pm 5 \text{ as}$ was measured, some 15 as larger than the $\sim 6 \text{ as}$ maximum delay predicted by a multi-electron model of the system under study. In view of its important implications, the true time origin for photoemission has motivated subsequent efforts towards the characterisation of the electron release as well as

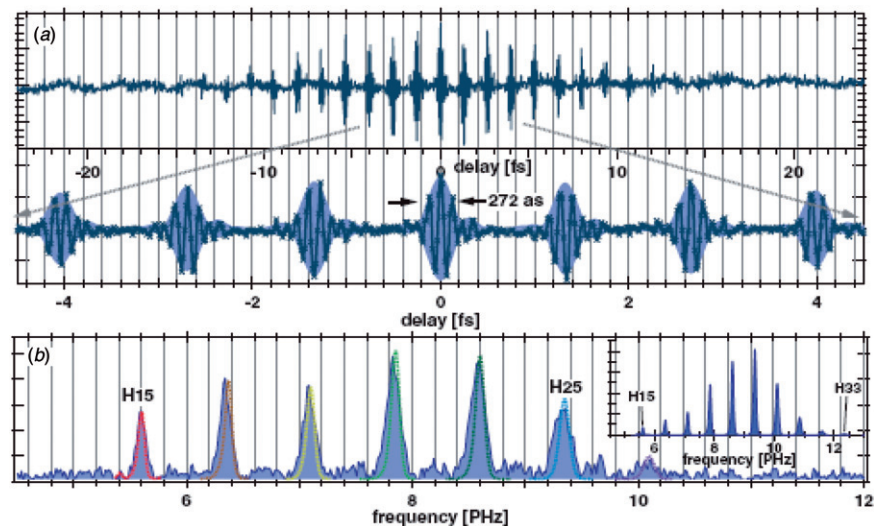


Figure 14. (a) Interference trace of the APT generated from Ar gas (top row) and a magnified view (bottom row). Cross markers correspond to the sampling points of scanned delay. (b) Magnitude of the Fourier transform of the APT interferometric trace, where the intensity has been arbitrarily normalised. Inset: observed intensity distribution in the XUV spectrograph. Reproduced with permission from Nabekawa et al. [82]. Copyright (2009) by the American Physical Society. (The colour version of this figure is included in the online version of the journal.)

the influence of the measurement process, the latter being invoked e.g. in [80]. The disentanglement of the single-photon ionisation time (Wigner time) and the delay inherent to the measurement process has been attained by means of an interferometric technique leading to a very satisfactory agreement between theory and experiment at high electron kinetic energy [81], where the influence of the core potential plays a minor role.

3. SAPs from multi-cycle driving sources

As described in Section 2, the time structure of the HHG signal when using multi-cycle driving pulses normally consists of attosecond pulse trains (APTs) with a period of half an optical cycle of the fundamental radiation (see experimental data in Figure 14). This makes it necessary to implement some type of gating technique if one would like to end up with a SAP from such a long driving field.

Using commercially available multi-cycle driving fields to generate SAPs represents a great advantage because such laser sources are found in many laboratories all over the world, and are relatively easily operated. With no need to run complicated few-cycle femtosecond laser sources involving complex schemes for extreme pulse compression and CEP-stabilisation, the attosecond science community could be enormously broadened to reach well beyond the borders of what is usually referred to as ultrafast/nonlinear

physics, to include also teams involved in ultrafast chemistry and biology.

These considerations have concentrated attention over the past five years on the possibility of SAP generation from multi-cycle fundamental sources. A number of schemes have been proposed and some of these also experimentally demonstrated. The most promising schemes and interesting and successful experiments are reviewed hereafter.

3.1. Double optical gating (DOG) and generalised double optical gating (GDOG)

If a second harmonic field is added to the fundamental frequency, it has been shown that the time-symmetry of the overall electric field is broken for specific relative phases between the two fields [83–85]. As a consequence, HHG can take place just once each full optical cycle of the fundamental field [19]. Double optical gating (DOG) [86] can be realised by combining the polarisation gating (PG) technique [72,74] with a two colour scheme [87], which has the advantage of relaxing the requirements for the minimal required temporal duration of the gate, from $T_L/2$ to T_L (see Figure 15).

By utilising such a scheme, based on a Mach–Zehnder interferometric combination of the driving beams [88] and on a collinear setup [89], a HHG continuum spectrum has been observed in the 26–36 nm range in argon and in the 20–28 nm range in neon [88] using a 9 fs NIR pulse. Similar results have

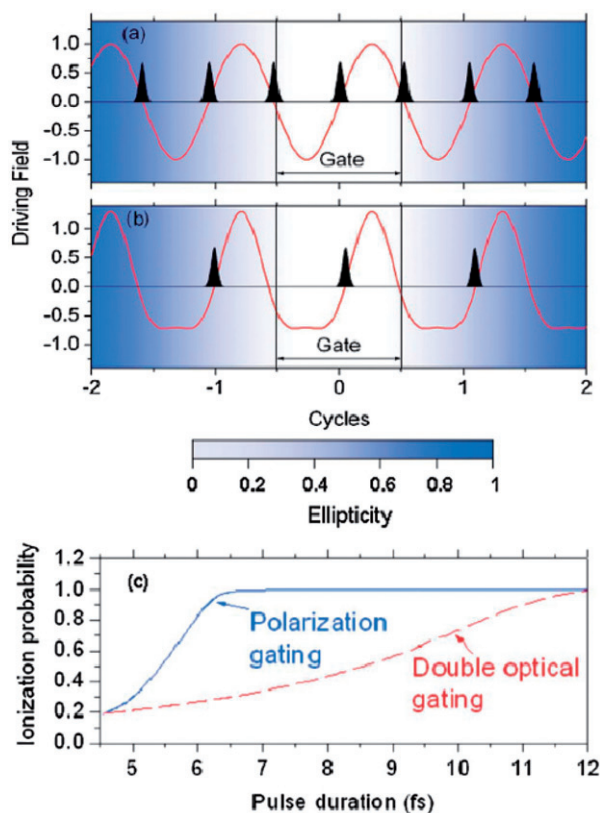


Figure 15. Principle of double optical gating (DOG). The driving field components for PG (a) without and (b) with the second harmonic field, respectively. The driving field is shown as the red line. The two vertical lines represent the gate width. Here, the filled curves are the attosecond pulses emitted when the driving fields alone are applied. The background colour shows the strength of the PG. In (c) the ionisation probability of an argon atom in the field of PG pulses is compared with that in the field of DOG. The longest pulses that can be used are those at which the probability reaches one. Reproduced with permission from Mashiko et al. [88]. Copyright (2008) by the American Physical Society. (The colour version of this figure is included in the online version of the journal.)

been obtained with an improved version of the setup [89]. Essentially the setup is based on the use of a birefringent quartz plate followed by an achromatic quarter-wave plate to produce the fundamental PG pulse. A BBO crystal placed in the other arm of the interferometer generates the second harmonic (SH) field. In these experiments the driving field needed to be CEP-stabilised, thus leading to the generation of continua of sufficient bandwidth to support the formation of 130 as long SAPs at the Fourier limit. In [88] it is demonstrated that PG also works under similar conditions to those used in the DOG scheme, but, interestingly, due to the much lower ionisation probability of the atom in the DOG scheme compared to the corresponding PG experiment (see Figure 15(c)), much higher effective intensities can be reached in the

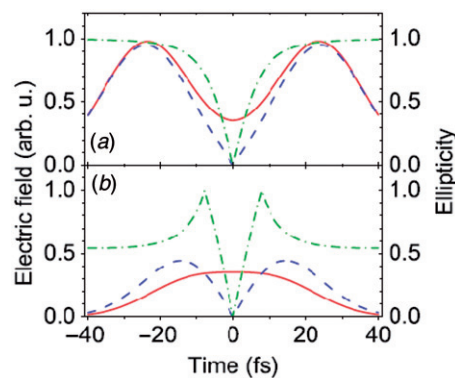


Figure 16. Comparison of the laser field components for polarisation gating in DOG (a) and GDOG (b). In both (a) and (b), the driving field and gating field are plotted in solid red line and dashed blue line, respectively, whereas the ellipticity is plotted in dash-dotted green line. Reproduced with permission from Feng et al. [90]. Copyright (2009) by the American Physical Society. (The colour version of this figure is included in the online version of the journal.)

gating for generating SAPs with DOG. This fact, together with the consequent reduction of the ground state depletion, results in a signal for the DOG which is 23 times higher than that of the corresponding PG, indicating a more intense SAP generation with DOG. It is worth noting that this SAP intensity enhancement has been achieved at the relatively moderate peak intensity of $\approx 3 \times 10^{14} \text{ W cm}^{-2}$.

A considerable step forward has been achieved through an important refinement of the DOG technique, known as generalised double optical gating (GDOG) [90], which allows one to generate SAPs from much longer multi-cycle pulses. Using the GDOG scheme (HHG in Ar) the generation of SAPs of 260 as duration from 20 fs laser pulses and 148 as pulses from 28 fs laser pulses, has been demonstrated [90]. The idea of GDOG is to relax the upper limit duration of the laser input pulse for efficient SAP isolation. In fact, if the laser pulse is too long, the atoms will be fully ionised by the leading edge, leaving no neutrals to emit attosecond pulses inside the polarisation gate, which is necessarily located at the peak of the overall pulse for DOG/GDOG schemes. Thus, to relax the requirement on the laser pulse duration, depletion of the atomic ground state has been reduced in GDOG by synthesising a polarisation gating field from two counter-rotating elliptically polarised pulses having ellipticity equal to ε , rather than circularly polarised pulses as in the DOG scheme. For a gate formed from elliptically polarised fields (see Figure 16), it can be shown that, if T_d is the time delay between the two field components, ε_{th} the so-called upper threshold ellipticity at which HHG is effectively terminated [91,92], and τ_p the laser

pulse duration, the polarisation gate width, δt_G , can be expressed as [88,93]:

$$\delta t_G \approx \varepsilon \frac{\varepsilon_{th} \tau_p^2}{\ln(2) T_d}. \quad (13)$$

Thus, for instance, if one chooses $\varepsilon_{th} = 0.2$ (as discussed in Section 2), for which the intensity of attosecond pulses generated outside the gate is expected to be at least 10 times lower than that of the main SAP, and sets $\tau_p = 20$ fs, then δt_G , equal to one optical cycle can be obtained by two combinations, i.e. $\varepsilon = 1$ (DOG) and $T_d = 48$ fs or $\varepsilon = 0.5$ (GDOG) and $T_d = 24$ fs. The latter case is shown in Figure 16, where the driving field amplitude inside the gate is kept the same for both cases.

Thus, in Figure 16 it is clear that while the gate width and the effective amplitude of the driving field are the same in DOG and GDOG, the amplitude of the overall field on the leading edge is much higher in DOG (Figure 16(a)) rather than GDOG (Figure 16(b)), with the advantage of a much reduced ionisation and ground state depletion of the generating medium in GDOG compared to DOG. As a consequence of the different gating scheme, the ellipticity outside of the gate is just 0.5 for GDOG versus 1 for DOG, but 0.5 should be sufficiently high to suppress SAP formation, possibly aided by the effects of harmonic field propagation through the medium (see Section 4).

The measured energy of the generated 260 as SAP was 0.23 nJ, and the SAP spectral bandwidth was 30–40 eV. FROG-CRAB was used to temporally characterise the SAP. The final measured pulse duration was consistently longer than the Fourier limit, due to a residual positive chirp of 7850 as², obtained from phase retrieval. A second attempt to generate SAP was also successful, when using 28 fs laser pulses directly from the chirped pulse amplifier, with no hollow fibre compressor stage. Even in this case, with suitable values of T_d , a 148 as SAP was characterised by FROG-CRAB. Moreover, by using the FROG-CRAB technique to characterise SAP satellites with half-cycle [94] and full-cycle [95] periodicity it was demonstrated that satellite pulses had an intensity 3 and 2 orders of magnitude lower than the main SAP for 20 fs and 28 fs driving pulses, respectively. This feature is very important since other methods to generate SAPs seem to have a much lower main pulse-to-satellite pulse contrast ratio [68], which may seriously compromise the usefulness of such light source to probe sub-fs dynamics.

An important recent work based on the GDOG scheme [96] reports on the possibility of making the gate sufficiently narrow to make SAP generation insensitive to the CEP value of the driving laser.

This is a great advantage in practice since relatively long-pulse multi-cycle lasers are often not CEP-stabilised. This result has been obtained by using 23 fs driving pulses and shaping a gate width of 1.4 fs, to be compared with 2.5–3 fs as used in [88]. As a consequence of such a short gate width, the CEP value only affects the SAP photon flux, not the pulse duration or contrast. It has been shown that the SAP photon flux can change by a factor of about 10 when the CEP value freely fluctuates in the 0– 2π range. The duration of the SAPs obtained in this case is about 180 as.

In concluding this section on DOG and GDOG methods, we stress that an intrinsic limitation here is due to the fact that the gate is always open at the peak of the overall driving pulse. The exciting results discussed so far, which indicate DOG/GDOG are very efficient methods to generate SAPs with long pulses, seem to be limited to peak intensities at focus in the $2\text{--}5 \times 10^{14} \text{ W cm}^{-2}$ range, which are lower than those achievable with multi-cycle driving lasers that typically have higher pulse energies in the several millijoules range. Higher laser pulse energy allows one to employ a larger interaction volume for HHG to optimise the phase-matching of the process. This can lead to a strong increase of the overall SAP signal from multi-cycle drive pulses. Therefore, the field is still open to the find a configuration which makes the best possible use of the high pulse energies available from multi-cycle lasers.

3.2. Polarisation gating and polarisation gating-like schemes with multi-cycle lasers

DOG and GDOG setups are relatively complicated, as one has to add a pump/probe two colour apparatus to the ordinary PG technique based on quarter waveplates [97]. Despite huge advances made using the GDOG technique in terms of the longest possible laser pulse duration able to generate SAPs (which is now compatible with ~ 30 fs commercial laser sources) and in terms of relaxing the constraint of using CEP-stabilised systems, GDOG is still limited by the requirement to wait for the top of the pulse to be reached, where SAP formation takes place. A solution to the above puzzle has been recently proposed in two schemes both based on the idea of mixing PG with interferometric techniques. A first attempt, which has been also experimentally demonstrated [98], is based on the use of a double Michelson interferometer (see Figure 17(a)).

Pulses from a 50 fs, 800 nm, 10 Hz repetition rate laser are split into two replicas by a first beam splitter. One replica enters a Michelson interferometer that introduces a delay T_d between the two arms so as to

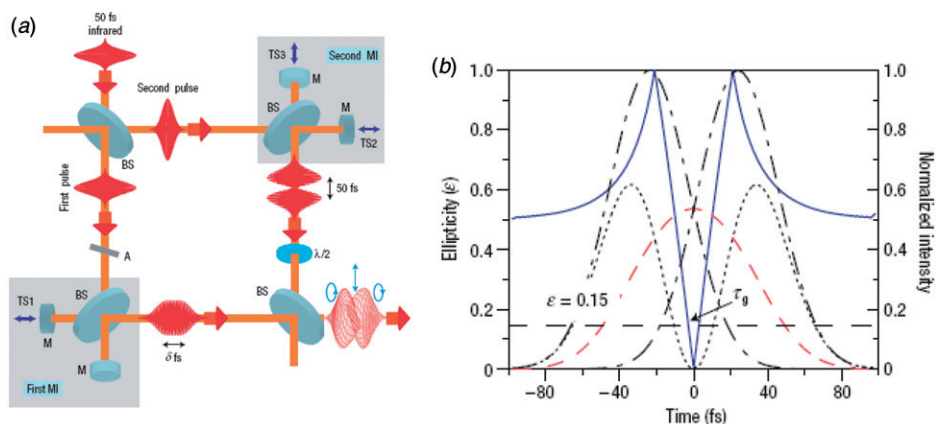


Figure 17. (a) Dual Michelson interferometer device. BS, beam splitter; M, flat mirrors, TS1,2,3: piezoelectric translation stages. A: intensity attenuator. First and second MI: first and second Michelson interferometer. (b) Solid blue line: ellipticity of the polarisation-modulated pulse used for the generation of XUV continua radiation. Black dashed-dotted line: normalised intensity of the two pulses, which partially overlap to form a pulse with a destructive interference minimum in its central part (black dotted line). Red dashed line: intensity distribution of the pulse showing the constructive interference maximum. For $\varepsilon = 0.15$ a time gate width of ~ 5 fs is obtained. Reproduced with permission from Tzallas et al. [98]. Copyright (2007) by Nature Publishing Group. (The colour version of this figure is included in the online version of the journal.)

induce a constructive interference maximum at the peak of the output pulse. The second replica enters a second Michelson interferometer which introduces a delay close to the initial pulse duration (~ 50 fs) so as to obtain destructive interference at the peak of the output pulse. The intensity of the first pulse can be adjusted by a variable attenuator whereas the polarisation of the second pulse is rotated by 90° by means of a half waveplate. Finally, the two pulses are recombined by a final beam splitter to give the time-dependent ellipticity, $\varepsilon(t)$, shown in Figure 17(b) as the blue solid line. For $\varepsilon = 0.15$ a time gate of nearly linear polarisation and $\delta t_G = 5$ fs results in the present case, located at the centre of the overall envelope. Under such conditions the authors observed in Ar the generation of XUV continua between 32 nm and 55 nm which is sufficient bandwidth to support a transformed limited SAP of 340 as. This approach has two substantial limitations to-date: (i) due to the lack of CEP stabilisation, it has not been possible to control XUV spectra on a single shot basis, and more importantly, (ii) since the gate is located at the centre of the final envelope, a strong, unavoidable ground state depletion occurs due to significant optical field ionisation on the leading edge of the pulse. This latter drawback, which also occurs when using DOG/GDOG schemes, implies that only a small fraction (≈ 10 – 20%) of the initial pulse energy can be actually used for SAP production.

The second recently proposed interferometric PG (IPG) scheme [99,100] has been predicted to efficiently work with NIR pulses as long as 20–25 fs. It relies on a single Michelson setup, but exploits the effect of

a frequency chirp induced by self phase modulation (SPM) taking place in a nonlinear material located in one of the two interferometer arms (see Figure 18(a)).

The final pulse exhibits two gates of linear polarisation, having a width of ≈ 2 fs, located in the leading and trailing edges of the pulse at about 70% of the peak intensity, as illustrated by the dashed blue line in Figure 18(b). Figure 18(c) shows the square of the electric field amplitude of the pulses coming from both the interferometer arms. As expected, the gates of linear polarisation correspond to times when the two fields are in phase. The second gate in the trailing edge cannot contribute to the final XUV signal when using an intense driving pulse, since ionisation depletes the atomic ground state, as shown by the solid green curve in Figure 18(b). This scheme offers a number of advantages over the former IPG scheme; the gate is very efficient, its duration can be modulated by imparting different amounts of SPM, and it is no longer open at the peak of the final pulse. In particular, the time location of the gate can be chosen whenever it is desired along the pulse: for instance, it can be placed to coincide with the highest possible intensity before ionisation can deplete the medium. For relatively long multi-cycle driving fields this is advantageous since the medium is no longer exposed to the long leading edge ‘waiting’ for the gate to open. This method has been predicted to produce ~ 370 as SAPs in the 20–40 nm spectral range. Propagation of driving and XUV fields plays a crucial role in the clean up the final XUV signal and the production of a SAP, as it will be discussed in Section 4 (and as illustrated in Figure 18(b)). The method is CEP-dependent, but its stability is found to

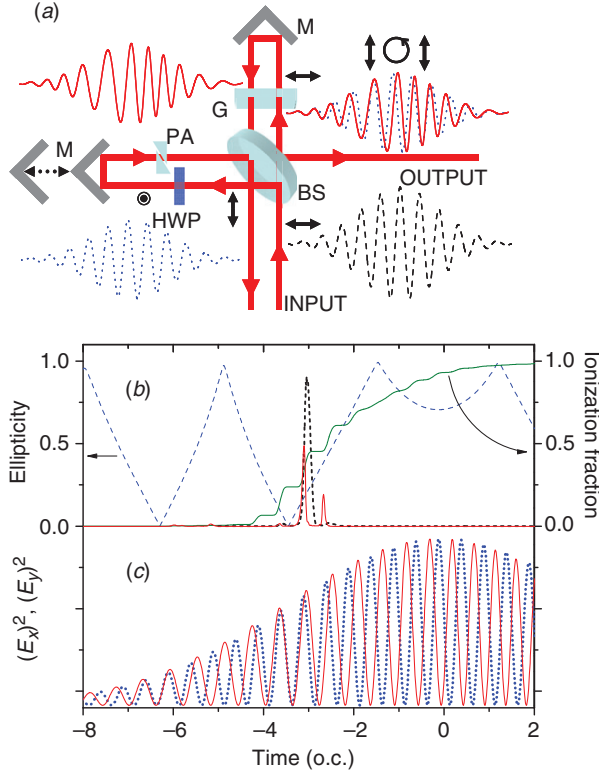


Figure 18. (a) Principle of the experimental scheme to realise interferometric polarisation gating. (b) Ellipticity (blue dashed line), ionisation fraction (solid green line), single dipole emission (red solid line), and near field emission (dashed black line) versus time for an initial pulse duration of 20 fs. The spectral filter adopted to select the SAP spectrum corresponds to window between the 20th to the 44th harmonic of the fundamental. (c) Chirped (E_y , solid red line) and chirp-free (E_x , dotted blue line) squared electric fields. Reproduced with permission from Altucci et al. [99]. Copyright (2008) by OSA. (The colour version of this figure is included in the online version of the journal.)

be relatively robust against CEP fluctuations. The SAPs obtained are predicted to be chirped, with a transform limited duration of ~ 150 as, and six times more intense [99] than SAPs obtained with few-cycle pulses [49,72].

An experimental implementation of the scheme proposed in [97] has been recently reported [101]. Single shot XUV continua in the 35–55 eV spectral range have been obtained in krypton by combining transform-limited 15 fs, 800 nm and orthogonally polarised chirped 35 fs, 800 nm pulses (see Figure 19). Continua are interpreted as the signature of the formation of a SAP and attributed to the interplay between polarisation, ionisation gating [102,103] and trajectory selection operated by suitable phase-matching conditions (see also Section 4).

A significant improvement achieved in [99] compared to the scheme proposed in [97] is the possibility

of chirping one of the two beams in order to realise polarisation gating by group delay dispersion (GDD) (rather than SPM) through the insertion of a suitable thickness of fused silica, as shown in Figure 20. This relaxes the requirement for significant SPM, which is not easy to achieve without significant temporal and spatial pulse distortion along the radial direction (orthogonal to propagation axis).

The right amount of chirp to be imparted in one of the arms of the interferometer corresponds to the best compromise between the need for a sufficiently steep polarisation gate, on the one hand, and not lengthening the chirped pulse too much, on the other hand. In this case the estimated linear chirp and GDD coefficients were $\alpha \approx 2.7 \times 10^{-3} \text{ fs}^{-2}$ and $\beta \approx 140 \text{ fs}^2$, respectively. Then, by assuming a Gaussian temporal shape for the driving pulses, the relation between α and β is given by:

$$\alpha = \frac{k^2 \beta}{2(\tau_p^4 + k^2 \beta^2)}, \quad (14)$$

where $k = 4 \ln 2$. Thus, for $\tau_p = 15$ fs Equation (14) predicts a maximum $\alpha \approx 3 \times 10^{-3} \text{ fs}^{-2}$, which is in fair agreement with the estimation for α , confirming optimal conditions in the experiment.

Moreover, high peak intensities ($\sim 8 \times 10^{14} \text{ W cm}^{-2}$) at the peak of the pulses have been used in [99], thus implying a very high intensity in the gate, estimated to be $\approx 5.5 \times 10^{14} \text{ W cm}^{-2}$, i.e. twice as high as that typically used in GDOG experiments.

The mechanism for SAP formation at work in the approach used in [99] is illustrated in Figure 21, which shows results of a simulation based on the strong field approximation [25], corresponding to the above experimental parameters. In particular, in Figure 21(b) it can be seen that a gate appears on the leading edge of the driving pulse, owing to the interplay between time modulation of the total electric field polarisation and ionisation depletion of the medium. As shown in Figure 21(c) both the single dipole response and final SAP are peaked in the gate located between 28 and 30 optical cycles. The gate is formed (see Figure 21(b)) by polarisation gating on the leading edge and by ionisation medium depletion, (i.e. ionisation gating) on the trailing edge. Interestingly, the ellipticity never falls below 0.4 within the gate, thus suggesting that in this scheme the usually accepted idea that the ellipticity in the gate must be in the range $0 \leq \varepsilon(t) \leq \varepsilon_{th} \approx 0.2$, does not hold anymore. It is possibly the ellipticity variation within the gate, $\Delta \varepsilon \approx 0.4$, rather than the value of $\varepsilon(t)$ that is responsible for temporal confinement in this case.

Figure 21(c) clearly indicates the formation of a SAP, lasting approximately 900 as after propagation

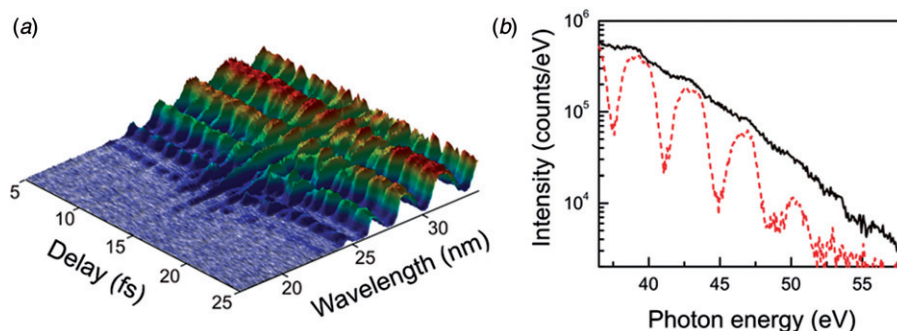


Figure 19. (a) Measured single-shot harmonic spectra in krypton for different delays between the short (15 fs) and the long (35 fs) pulse. (b) Single-shot harmonic spectra generated in krypton for delays of 15 fs (solid curve) and 15.5 fs (dashed curve), respectively between short and long driving pulse (short pulse ahead). Reproduced with permission from Altucci et al. [101]. Copyright (2010) by OSA. (The colour version of this figure is included in the online version of the journal.)

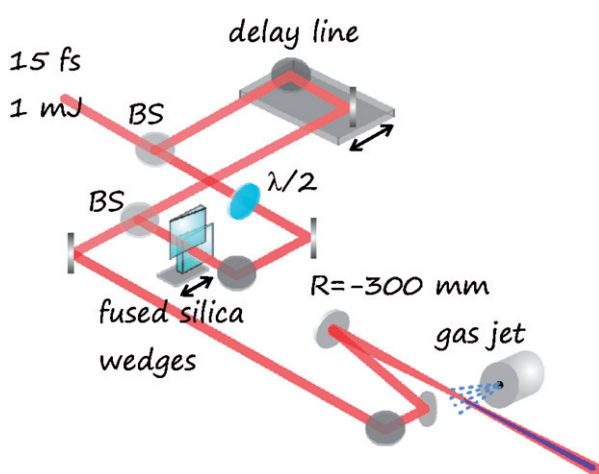


Figure 20. Layout of the experimental setup used in [101]. BS corresponds to beam splitter, $\lambda/2$ corresponds to half-wave plate. (The colour version of this figure is included in the online version of the journal.)

of the signal to the far field. Again a key role in the SAP formation mechanism is played by propagation through the target. In absence of propagation, the single dipole response is made of three distinct pulses associated with the recombination originating from three different electron trajectories [100]. It is important to note that this method requires a CEP stabilisation within $\approx 150\text{--}200$ mrad rms for robust SAP formation.

3.3. Other two-colour schemes and synthesised fields

Besides the DOG and GDOG methods, other schemes have been recently implemented aimed at SAP generation, which are based on a two-colour ultrashort laser source having multi-cycle pulse duration. For example in [87], a two-colour laser field consisting of a sub-10 fs fundamental wavelength and its parallel-polarised

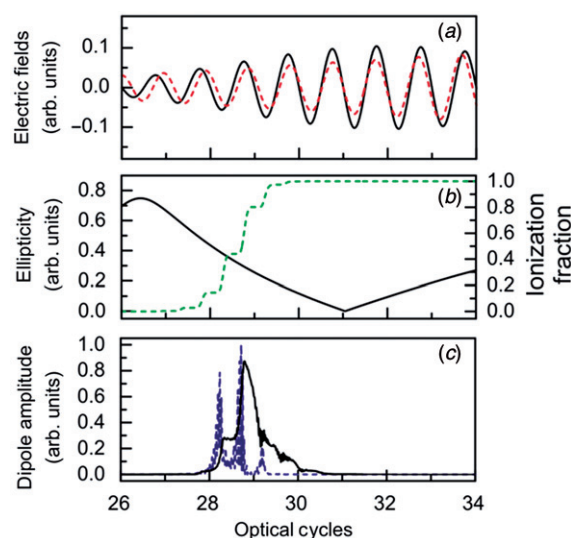


Figure 21. (a) Calculated perpendicularly polarised components of the electric field: 15 fs 750 nm pulse (dashed curve) and chirped 33 fs 750 nm pulse (solid curve). (b) Calculated ellipticity of the total driving field (solid curve, left vertical scale) and ionisation fraction in krypton based on non-adiabatic ADK rates [104] (dashed curve, right vertical scale). (c) Calculated single dipole response (dashed curve) and propagated harmonic field in the far field (solid curve). The parameters of the simulations are: a delay of 15 fs between the two pulses with the short pulse ahead, a CEP value of $\pi/8$ rad and $-\pi/8$ rad for the short and the long pulse, respectively, a peak intensity of about $8 \times 10^{14} \text{ W cm}^{-2}$ for both pulses and a GDD of $\approx 180 \text{ fs}^{-2}$ for the chirped pulse. As for the gas jet the local pressure is 25 mbar, the length 0.6 mm, the jet being positioned 1 mm after focus in the diverging beams with a confocal parameter of 2.4 mm. Reproduced with permission from Altucci et al. [101]. Copyright (2010) by OSA. (The colour version of this figure is included in the online version of the journal.)

second harmonic was used to drive HHG in argon. A ≈ 9 nm wide continuum spectrum centred at 30 nm was obtained on a single shot basis, carrying an overall energy as high as 10 nJ. The observation was restricted

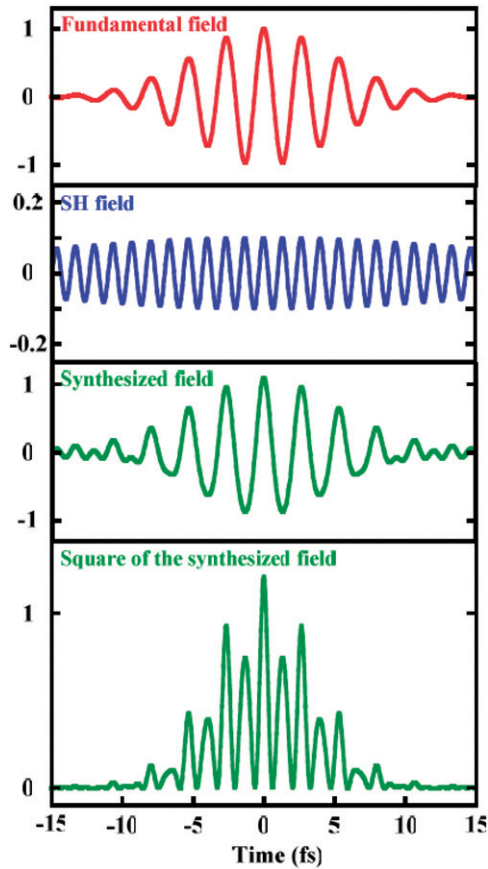


Figure 22. Temporal profile of the fundamental, second harmonic and synthesised electric fields and the square of the synthesised electric field. The amplitudes of the fundamental and second harmonic fields are 0.9 and 0.1 arbitrary units, respectively. Reproduced with permission from Oishi et al. [87]. Copyright (2006) by OSA. (The colour version of this figure is included in the online version of the journal.)

to the single-shot regime (as in the IPG method described above), since this SAP generation mechanism is expected to require CEP stabilisation, and the laser source was not CEP-stabilised in [87]. The Fourier limit of the generated continuum corresponds to ~ 200 as. Due to symmetry breaking in the presence of the second harmonic field, the HHG spectrum consists of both even and odd harmonics. For sub-10 fs driving pulses, the bandwidth of these is sufficiently broad for them to overlap to form a quasi-continuum. The time counterpart of this can be understood as a reshaping of the electric field, resulting in a shortening of the effective pulse duration that contributes to HHG [105,106]. This is illustrated in Figure 22 for first and second harmonic field amplitudes in the ratio 9:1, as used in [87].

Recently, another two-colour scheme has been implemented in which an 800 nm, 30 fs pulse was mixed with a 1300 nm (mid-IR, tuneable in principle), 40 fs

pulse [107]. The intensity ratio used in the experiment between the main 800 nm and the 1300 nm field was 1:0.15, $1.15 \times 10^{14} \text{ W cm}^{-2}$ being the overall peak intensity. The idea of the authors here is that by adjusting the wavelength of the supplementary 1300 nm field a suppression is obtained of the multiple burst pulse of the overall two-colour field so as to successfully generate a SAP. Moreover, an extension of the HHG cut-off is achieved due to the addition of the mid-IR field, while still keeping low the ground state depletion of the atomic target. In fact, the cut-off energy becomes in this case [108]

$$E_{\text{HHG}} \approx I_P + 3.17U_{P0} \left(1 + 1.6\sqrt{\xi}\omega_0/\omega_1 \right) + 3.17U_{P1}, \quad (15)$$

where ξ is the intensity ratio between the 1300 nm/800 nm fields, and ω_0 and ω_1 are the frequencies of the main and the mid-IR field, respectively. Thus, compared with Equation (1), two new terms appear in Equation (15), by adding the mid-IR field, $3.17U_{P0} \cdot 1.6\sqrt{\xi}\omega_0/\omega_1 + 3.17U_{P1}$, which increases the cut-off energy thus making possible shorter SAPs. Moreover, the authors claim that there is no need for CEP stabilisation of the laser source since CEP fluctuations only affect the SAP intensity and not the SAP formation. Simulations based on single dipole calculations followed by propagation of the driving and the harmonic fields indicate that satellite attosecond pulses are generated as well, but their peak intensity does not exceed 6% of the main peak intensity under optimised conditions. The generation of SAPs of ~ 500 as is predicted, corresponding to the 59–67 eV bandwidth.

Another very interesting gating technique to produce SAPs has been recently proposed [109] which relies on the mixing of two or three multi-cycle laser pulses at incommensurate frequencies. In such a way the sub-cycle shape of the overall electric field is modified so as to lead to SAP generation. The idea, theoretically proposed in [110,111], is based on the fact that the addition of a second, ω_2 , and possibly a third optical field whose frequency is not commensurate with the primary field, ω_1 , can create additional frequency components, Ω . Depending on the frequency ratio between the fields, this can result in a quasi-continuous spectrum in the harmonic plateau region, according to the following selection rules [109]:

$$\Omega = n_1\omega_1 + n_2\omega_2, \quad n_1 + n_2 = 2k - 1, \quad n_1, n_2, k \in \mathbb{Z} \quad (16)$$

where n_1 , n_2 are the photon numbers in the primary and second field, respectively, producing the XUV Ω component. An example of the creation of the new

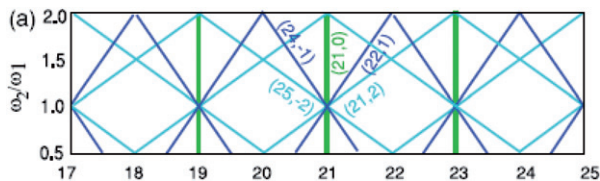


Figure 23. Schematic of the positions of the frequency components predicted by the model [109]. The horizontal axis here is the emitted XUV frequency normalised to the intense OPA laser frequency ω_1 . Thus, $n_2=0$ (green vertical lines) corresponds to the usual single-frequency case which gives the odd harmonics of ω_1 . The dark blue slightly tilted lines and the light blue tilted lines correspond to the $n_2=1$ and $n_2=2$ cases, respectively. Reproduced with permission from Bandulet et al. [109]. Copyright (2010) by the American Physical Society. (The colour version of this figure is included in the online version of the journal.)

frequencies is shown in Figure 23 where the ω_2 -field is chosen to be a relatively weak 800 nm component and the wavelength corresponding to the ω_1 -field is the intense output field of an optical parametric amplifier (OPA), variable in the range 1200–1500 nm.

It is predicted [109] that the density of peaks will increase as the two laser frequencies become closer to one another, $\omega_2 \rightarrow \omega_1$. The case experimentally investigated in [107] corresponds to $\omega_2/\omega_1=0.81$, which is obtained by combining the OPA signal at 1450 nm with an intensity of $3 \times 10^{14} \text{ W cm}^{-2}$ and the idler at 1785 nm with an intensity of $1.5 \times 10^{14} \text{ W cm}^{-2}$. It is reported [107] that with no delay between signal and idler a continuous spectrum is measured for Ω/ω_1 in the range 15–32.

Another attempt combined three fields together, a strong harmonic-generating field at 1325 nm with two weak fields at 800 and 2020 nm, to tailor an overall field which is more efficient for SAP generation. Even in this case the spectrum becomes quasi-continuous. The OPA used in [107] was seeded by superfluorescence, thus the three frequencies were not phase-locked and their combination cannot yield SAPs. However, OPAs that use white light generation to produce the seed for the signal wavelength can have all three frequencies phase-locked [66]. It should thus be possible to produce SAPs from multi-cycle pulses by employing this method, as shown by the single dipole calculation reported in Figure 24 [107], where three fields centred at 800, 1300, and 2080 nm are combined with correct relative phases so as to produce a SAP. Physically, SAPs here are generated because of electric field time-symmetry breaking.

3.4. Ionisation gating

The idea to use an ionisation gating mechanism to produce continuum emission of high-harmonics on the

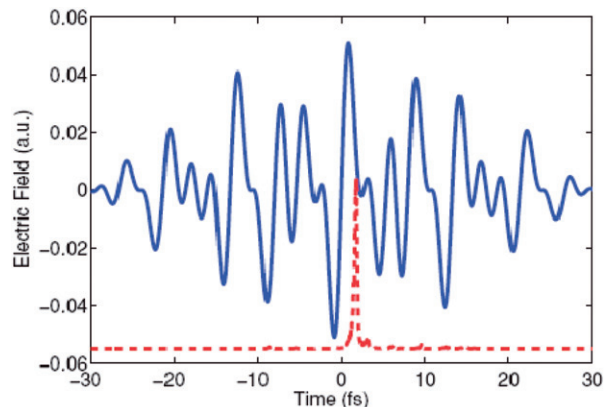


Figure 24. Electric field resulting from the combination of three fields corresponding to 800, 1300 and 2080 nm (blue solid line). Each field has a Gaussian envelope with an intensity FWHM of 24 fs and an amplitude of 0.02 a.u. The dashed red line (vertically shifted) shows the calculated XUV intensity by solving the time-dependent Schrödinger equation with a smoothed hydrogen-like potential. The relative phase was such that all three fields are sine-like at the peak of the envelope, which resulted to be the optimum condition for SAP generation. Propagation was not accounted for. Reproduced with permission from Bandulet et al. [109]. Copyright (2010) by the American Physical Society. (The colour version of this figure is included in the online version of the journal.)

leading edge of the driving laser pulse, indicative of a SAP formation, was originally presented in [112]. It was first observed that laser-induced ionisation can be used to shorten the harmonic pulse duration for a single harmonic order [113,114]. More recently, it has been found that a gating mechanism driven by a strong ionisation of the medium on the leading edge of the pulse can also lead to the generation of XUV continua, associated with SAP formation [101,115]. The essential idea is to restrict the harmonic emission to only one or two half-cycles on the leading edge of an intense driving pulse, because of ionisation gating which depletes the medium along the rest of the pulse, thus enabling SAP production. However, as introduced in Section 2, a deeper analysis of the results showed that the basic mechanism is due to ionisation-induced phase-mismatching between the fundamental and the harmonic beams [101]. This finding turns attention to *macroscopic* rather than *microscopic* effects, highlighting the extremely important role played by harmonic propagation through the medium in SAP formation when using multi-cycle driving pulses. By this method, continuous harmonic spectra between 90 and 100 eV have been observed [101] when a 7 fs, 800 nm intense pulse ($7 \times 10^{14} \text{ W cm}^{-2}$) was focused in a neon target. Theoretical predictions [111] indicate that the scheme should work also with much longer 21 fs pulses having a peak intensity as high as $2 \times 10^{15} \text{ W cm}^{-2}$.

This method is found to be strongly CEP-dependent, thus requiring a CEP-stabilised source to operate properly. Recently, under conditions similar to the those cited above and used in [101] it has been demonstrated that the temporal structure of the XUV signal consists of a main attosecond pulse preceded by a smaller satellite [116]. The contrast ratio between the amplitude of main/satellite pulse is found to be CEP-dependent as well and measured to be 2.7 ± 0.3 in the best possible case for CEP = 0, π rad.

3.5. Summary

As a summary of Section 3 we would like to group the essential features of the illustrated methods to generate SAPs from multi-cycle fundamental lasers in Table 1 which could be useful for researcher to help them choose the best possible option according to their specific requirements. We summarise the reviewed methods reporting their characteristics as found in the literature. Where no mention is made in the literature of a specific parameter we leave it blank.

4. Role of propagation

Initially it was thought that the essential physical mechanisms for SAP generation were all contained in the single atom response to an ultrashort and intense driving field. This was also believed to be the case when using PG schemes on the basis of previous tests with multi-cycle fundamental pulses [117] until it became clear that propagation of both the fundamental and the XUV fields through the nonlinear gaseous target plays an essential role in the attosecond pulse formation [91,118] (see also [119] for a review on macroscopic aspects of attosecond pulse generation).

The role of propagation is particularly striking when looking at PG applied to few-cycle driving fields as demonstrated in [120]. In fact, in this case the ellipticity of the driving field changes significantly on the single optical cycle time-scale which implies a much longer single atom response than expected, as shown in Figure 25(a) for conditions similar to those used in [51,74]. For both the investigated CEP values, 0 and $\pi/2$, the single atom emission consists of a complicated sequence of bursts lasting about two optical cycles (≈ 5 fs for a carrier wavelength of 800 nm), which is a much longer window than the corresponding $\delta t_G \approx 1.1\text{--}1.2$ fs for $\varepsilon_{th} \approx 0.2$, and should not allow SAP formation. Nevertheless, the corresponding final XUV signal delivered as a macroscopic emission from the whole gas target (thus reflecting the effect of

fundamental and harmonic field propagation), is a short SAP, as shown in Figure 25(b) and (c). In Figure 25(b) the on-axis final signal is plotted versus time, whereas in Figure 25(c) the temporal behaviour of the overall XUV pulse is reported. For a CEP of $\phi = \pi/2$, the final signal is a SAP lasting approximately a quarter of a cycle (≈ 300 as), whereas for $\phi = 0$ two attosecond pulses separated by slightly less than half a cycle are generated. Three-dimensional propagation of the NIR and the harmonic field acts as an efficient filter that “kills” a number of electron trajectories which contribute to the single atom emission, as first reported in [121] for ‘conventional’ HHG driven by few-cycle pulse with no use of PG. The key point is that these radiation contributions to the XUV field vary in phase depending on where in the medium and when during the driving pulse they have been emitted and thus, during propagation, they are not efficiently phase-matched and finally cancel out.

A classical trajectory study of the active electron reveals the existence of *superlong* trajectories in this specific case, which are responsible for the surprisingly long-lasting single atom emission. An example of such a trajectory [120] is reported in Figure 26 for $\phi = 0$, but similar superlong trajectories can be found also for other CEP values.

The active electron in Figure 26 was born in the continuum at $t_{birth} = 0.038$ optical cycles, when the ellipticity has a value $\varepsilon(t_{birth}) = 0.032$. The electron recollides at $t_{rec} = 1.44$ optical cycles (corresponding to 3.67 fs at a carrier wavelength of 800 nm) when the instantaneous ellipticity is very large, being $\varepsilon(t_{rec}) = 0.83$. The final energy of the recolliding electron is about 28 eV, which corresponds well with the spectral window of the generated SAP. The trajectory exhibits a large overall spatial excursion of more than 2 nm in the x - and about 1.5 nm in the y -direction and starts with zero initial velocity. The dashed red line shows the classical trajectory one would obtain under the same conditions, but with a constant ellipticity of 0.032. Thus, with a slowly changing ellipticity, even a small value of ε ensures that the electron never recombines, whereas with an ellipticity changing on the optical period time-scale, recombination is possible even for $\varepsilon \approx 0.5\text{--}0.6$, giving rise to superlong trajectories. Fortunately, propagation filtering makes possible the generation of well-behaved SAPs even in this context.

Propagation plays an essential role even for SAP generation from multi-cycle sources. This has been clearly shown in [100] for a PG scheme which makes use of 20 fs, 800 nm pulses, based on the experimental scheme proposed in [99] and realised in [101]. In this case, the analysis of the single dipole response along the propagation axis indicates that emitted radiation

Table 1. Summary of methods to generate SAPs from multi-cycle lasers.

Name of the method	SAP duration (as)	Spectral bandwidth (eV)	Brightness	Satellite/main contrast ratio	Duration/intensity of fundamental pulses	Technical difficulty/miscellaneous comments	Limitations
GDOG (generalised double optical gating)	150–200 (measured)	30–40 (measured)	Very high; $\sim 20 \times$ higher than PG methods	10^{-2} (measured)	$20\text{--}30\text{ fs}/3\text{--}4 \times 10^{14}\text{ W cm}^{-2}$ (measured)	Not too difficult. CEP-independent in its latest versions	Not applicable with intensities $\geq 5 \times 10^{14}\text{ W cm}^{-2}$
Polarisation gating (PG) – interferometric (dual Michelson)	340 (estimated)	23–40 (measured)	–	–	$50\text{ fs}/1\text{--}2 \times 10^{14}\text{ W cm}^{-2}$	Quite complicated. CEP-dependent	Not applicable with intensities $\geq 2 \times 10^{14}\text{ W cm}^{-2}$, with pulse duration as long as 50 fs
Polarisation gating (PG) – interferometric	380 (predicted) 900 (measured)	35–55 (predicted and measured)	High; predicted to be $\sim 6 \times$ higher than few-cycles methods.	10^{-1} (predicted)	$25\text{ fs}/7 \times 10^{14}\text{ W cm}^{-2}$ (predicted) $15\text{ fs} + 35\text{ fs}$ (measured)	Relatively easy to implement CEP-dependent (not critically)	Not applicable with laser pulses longer than 25–30 fs
TC (Two-colour) mid-IR	< 500 (estimated)	59–67 (measured)	–	10^{-1} (estimated)	$30\text{--}40\text{ fs}$ (measured)/ $\sim 1 \times 10^{14}\text{ W cm}^{-2}$ (measured)	Easy to implement (but requires an OPA). Partially CEP-dependent	Requires specific wavelengths to work, otherwise has few limitations
Multi-colour (two/three-colour) mid-IR incommensurate frequencies	< 1000 (estimated)	50–60 (estimated and measured)	–	–	25 fs (measured)/ $\sim 1\text{--}3 \times 10^{14}\text{ W cm}^{-2}$ (measured)	Easy to implement (but requires an OPA). Sensitive to the relative phases between the colours	Requires specific wavelengths to work and OPAs that use white light generation to produce the seed for the signal wavelength. Otherwise, has few limitations
Ionisation gating	< 1000 (estimated)	85–95 (measured)	–	0.3 (measured), CEP-dependent	7 fs (measured) 21 fs (predicted)/ $7 \times 10^{14}\text{ W cm}^{-2}$ (measured) $2 \times 10^{15}\text{ W cm}^{-2}$ (predicted)	Easy to implement. Strongly CEP-dependent	Requires CEP-stabilised fields, otherwise has few limitations

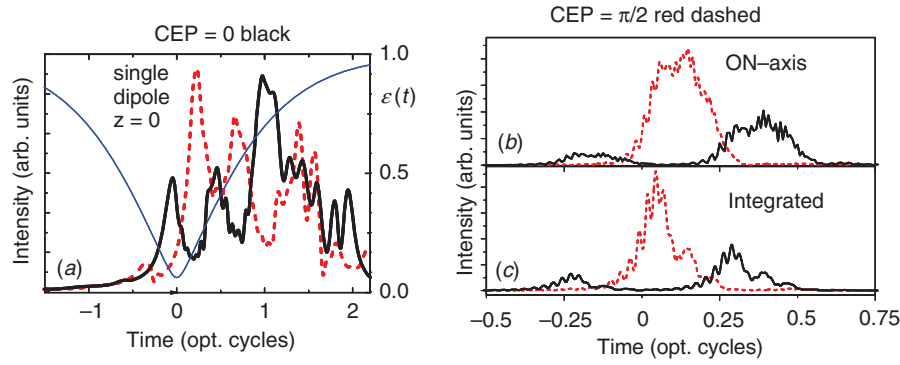


Figure 25. (a) Time behaviour of argon single dipole emission filtered within the 25–45 eV spectral range for CEPs of 0 (black, thick solid line) and $\pi/2$ rad (red, dashed line). The laser pulse time-dependent ellipticity is reported (blue, solid line). (b) Near-field, on-axis propagated harmonic intensity obtained in the same conditions of dipole emission as (a). (c) Same as in (b) but 3D integrated. The CEP values are 0 rad and $\pi/2$ rad for solid and dashed lines, respectively. Reproduced with permission from Altucci et al. [120]. Copyright (2007) by the American Physical Society. (The colour version of this figure is included in the online version of the journal.)

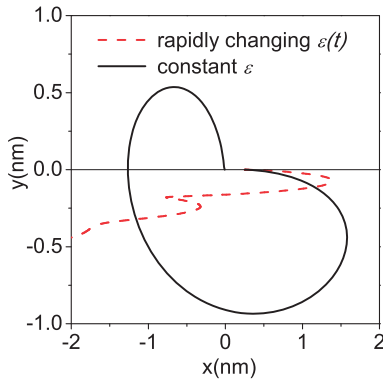


Figure 26. Superlong classical trajectory of an Ar electron which tunnels out through the Ar dynamic potential barrier at $x=0.25$ nm, $y=0$ with zero initial velocity (solid black line). The laser pulse parameters in the simulations are 5 fs, 800 nm, and a peak intensity of $\approx 5 \times 10^{14}$ W cm $^{-2}$. The red-dashed line displays the trajectory that the active electron would follow if the ellipticity were frozen on the optical cycle time scale at the ionisation time value of $\xi=0.032$. The final energy of the recombining electron is 28 eV in both cases. Reproduced with permission from Altucci et al. [120]. Copyright (2007) by the American Physical Society. (The colour version of this figure is included in the online version of the journal.)

consists of three main bursts, labelled as B1, B2, and B3 in the time interval $(-4T_L, -2T_L)$. At the entrance of the gas medium the emission is confined in this time interval because of the combined effect of a polarisation gate and ionisation. Indeed, near the entrance of the medium the ground state is fully depleted towards the pulse centre. For inner regions of the gas target, the dipole response changes and these modifications are roughly proportional to the distance travelled into the medium, which is an indication of the importance of propagation effects.

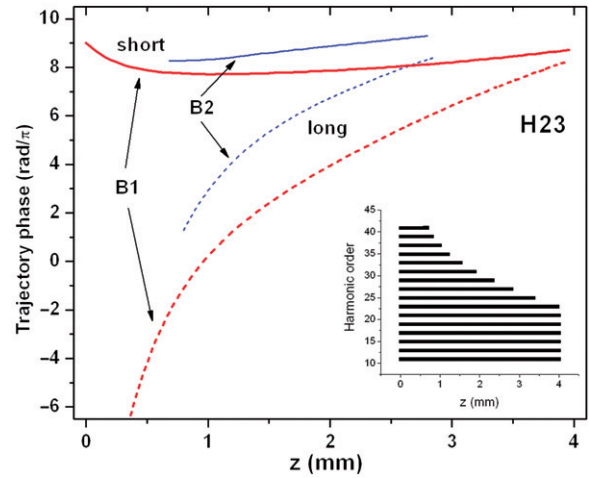


Figure 27. Phases of the trajectories generating H23, on-axis, versus the propagation direction. Short and long trajectories contributing to the B1-burst, emitted at $t=-3.1T_0$, and to the B2-burst, emitted at $t=-2.6T_0$ are included. The inset shows the extension of the trajectories generating the harmonics from H11 to H41. Reproduced with permission from Tosa et al. [100]. Copyright (2009) by OSA. (The colour version of this figure is included in the online version of the journal.)

A quantum trajectory calculation [102,122] performed within the saddle-point approximation [100], reveals the detailed mechanism of SAP formation, helping to understand the burst selection during propagation and the dependence of this process on the birth time of the radiation burst. In Figure 27 the phases of classical trajectories are plotted versus the propagation distance, z , for the 23rd order harmonic (H23). Both trajectories contributing, originating from B1 and B2 bursts, are plotted. One can immediately see that only the phases of the short trajectories [123] in the

B1 burst fulfil the condition for good phase-matching for propagation of H23. The coherence length, L_{coh} (see Section 2), is initially 0.4 mm, but for z in the range 0.5–2 mm is larger than 2 mm which indicates that B1 is well phase-matched. In addition, quantum trajectory analysis clarifies the origin of different bursts. The B1-burst is built from short trajectories which survive along the whole propagation distance and this explains its high intensity. The B2-burst develops only in a limited range of the gas target from short trajectories which have larger phase variation, this being the reason why it is weaker in intensity.

5. Conclusions

In this paper we have reviewed the principal techniques available to date to generate and characterise single attosecond pulses (SAPs). The SAP sources described in this paper are those based on the high harmonic generation in noble gases driven by femtosecond lasers. We considered SAP generation schemes using few-cycle, CEP stabilised drive pulses and schemes based on multi-cycle pulses. Few-cycle schemes lead to the generation of the shortest SAPs (~ 80 as), but require complex laser systems that are currently found in only a relatively small number of laboratories. The generation of SAPs from multi-cycle lasers, including those without CEP-stabilisation, has been demonstrated through a variety of approaches, and pulses lasting approximately 200–300 as have been generated. Such lasers are less complex and far more widespread than their few-cycle counterparts and usually offer higher pulse energies. This has the potential to open up attosecond science to a much broader community of scientists, and to unlock applications that require higher SAP fluxes.

We have reviewed the main methods of SAP generation from multi-cycle lasers, concentrating on techniques that have been experimentally demonstrated. This included two-colour schemes such as DOG and GDOG, PG and PG-like experiments, the ionisation gating extension to the multi-cycle regime, and recent attempts based on the use of synthesised fundamental fields. We stressed the fundamental role that collective effects, such as phase-matching through the medium, have in generating clean single attosecond pulses; in fact, although single atom response can properly account for many features of the final XUV pulse (e.g. the spectrum), it is only when the contributions arising from the several atoms in the medium are added up and their phase is considered that the experimental findings and the efficiency of the process are well reproduced.

Acknowledgements

CA and RV acknowledge V. Tosa, J. Marangos, S. Stagira, and C. Vozzi for valuable discussions. JWGT acknowledges the support of the Engineering and Physical Sciences Research Council (EP/F034601/1) and the assistance of C. Arrell, F. Frank, W. Okell and T. Witting.

References

- [1] McPherson, A.; Gibson, G.; Jara, H.; Johann, U.; Luk, T.S.; McIntyre, I.A.; Boyer, K.; Rhodes, C.K. *J. Opt. Soc. Am. B* **1987**, *4*, 595–601.
- [2] Ferray, A.; L’Huillier, A.; Li, X.F.; Lompre, L.A.; Mainfray, G.; Manus, C. *J. Phys. B* **1988**, *21*, L31–L35.
- [3] Pfeifer, T.; Spielmann, C.; Gerber, G. *Rep. Prog. Phys.* **2006**, *69*, 443–505.
- [4] Farkas, G.; Tóth, C. *Phys. Lett. A* **1992**, *168*, 447–450.
- [5] Paul, P.M.; Toma, E.S.; Breger, P.; Mullot, G.; Augé, F.; Balcou, P.; Muller, H.G.; Agostini, P. *Science* **2001**, *292*, 1689–1692.
- [6] Hentschel, M.; Kienberger, R.; Spielmann, C.; Reider, G.A.; Milosevic, N.; Brabec, T.; Corkum, P.; Heinzmann, U.; Drescher, M.; Krausz, F. *Nature* **2001**, *414*, 509–513.
- [7] Marangos, J.P.; Baker, S.; Kajumba, N.; Robinson, J.S.; Tisch, J.W.G.; Torres, R. *Phys. Chem. Chem. Phys.* **2008**, *10*, 35–48.
- [8] Altucci, C.; Velotta, R.; Marangos, J.P. *J. Mod. Opt.* **2010**, *57*, 916–952.
- [9] Khan, S. *J. Mod. Opt.* **2008**, *55*, 3469–3512.
- [10] Berrah, N.; Bozek, J.; Costello, J.T.; Dusterer, S.; Fang, L.; Feldhaus, J.; Fukuzawa, H.; Hoener, M.; Jiang, Y.H.; Johnsson, P.; Kennedy, E.T.; Meyer, M.; Moshhammer, R.; Radcliffe, P.; Richter, M.; Rouzée, A.; Rudenko, A.; Sorokin, A.A.; Tiedtke, K.; Ueda, K.; Ullrich, J.; Vrakking, M.J.J. *J. Mod. Opt.* **2010**, *57*, 1015–1040.
- [11] Agostini, P.; DiMauro, L.F. *Rep. Prog. Phys.* **2004**, *67*, 813–855.
- [12] Scrinzi, A.; Ivanov, M.Y.; Kienberger, R.; Villeneuve, D.M. *J. Phys. B* **2006**, *39*, R1–R37.
- [13] Corkum, P.B.; Krausz, F. *Nat. Phys.* **2007**, *3*, 381–387.
- [14] Kling, M.F.; Vrakking, M.J.J. *Annu. Rev. Phys. Chem.* **2008**, *59*, 463–492.
- [15] Krausz, F.; Ivanov, M. *Rev. Mod. Phys.* **2009**, *81*, 163–234.
- [16] Kulander, K.; Schafer, K.; Krause, J. *Super-Intense Laser-Atom Phys. B* **1993**, *316*, 95–110.
- [17] Corkum, P.B. *Phys. Rev. Lett.* **1993**, *71*, 1994–1997.
- [18] Antoine, P.; L’Huillier, A.; Lewenstein, M. *Phys. Rev. Lett.* **1996**, *77*, 1234–1237.
- [19] Mauritsson, J.; Johnsson, P.; Gustafsson, E.; L’Huillier, A.; Schafer, K.J.; Gaarde, M.B. *Phys. Rev. Lett.* **2006**, *97*, 013001.
- [20] Salières, P.; Carré, B.; Le Déroff, L.; Grasbon, F.; Paulus, G.G.; Walther, H.; Kopold, R.; Becker, W.;

- Milošević, D.B.; Sanpera, A.; Lewenstein, M. *Science* **2001**, *292*, 902–905.
- [21] Mairesse, Y.; de Bohan, A.; Frasiniski, L.J.; Merdji, H.; Dinu, L.C.; Monchicourt, P.; Breger, P.; Kovačev, M.; Taieb, R.; Carré, B.; Muller, H.G.; Agostini, P.; Salières, P. *Science* **2003**, *302*, 1540–1543.
- [22] López-Martens, R.; Varjú, K.; Johnsson, P.; Mauritsson, J.; Mairesse, Y.; Salières, P.; Gaarde, M.B.; Schafer, K.J.; Persson, A.; Svanberg, S.; Wahlström, C.-G.; L’Huillier, A. *Phys. Rev. Lett.* **2005**, *94*, 033001.
- [23] Baker, S.; Robinson, J.S.; Haworth, C.A.; Teng, H.; Smith, R.A.; Chirilă, C.C.; Lein, M.; Tisch, J.W.G.; Marangos, J.P. *Nature* **2006**, *312*, 424–427.
- [24] Baker, S.; Robinson, J.S.; Lein, M.; Chirilă, C.C.; Torres, R.; Bandulet, H.C.; Comtois, D.; Kieffer, J.C.; Villeneuve, D.M.; Tisch, J.W.G.; Marangos, J.P. *Phys. Rev. Lett.* **2008**, *101*, 053901.
- [25] Lewenstein, M.; Balcou, P.; Ivanov, M.Y.; L’Huillier, A.; Corkum, P.B. *Phys. Rev. A* **1994**, *49*, 2117–2132.
- [26] Lewenstein, M.; Salières, P.; L’Huillier, A. *Phys. Rev. A* **1995**, *52*, 4747–4754.
- [27] Antoine, P.; L’Huillier, A.; Lewenstein, M.; Salières, P.; Carré, B. *Phys. Rev. A* **1996**, *53*, 1725–1745.
- [28] Dietrich, P.; Burnett, N.H.; Ivanov, M.; Corkum, P.B. *Phys. Rev. A* **1994**, *50*, R3585–R3588.
- [29] Burnett, N.H.; Kan, C.; Corkum, P.B. *Phys. Rev. A: At. Mol. Opt. Phys.* **1995**, *51*, R3418–R3421.
- [30] Budil, K.S.; Salières, P.; Perry, M.D.; L’Huillier, A. *Phys. Rev. A* **1993**, *48*, R3437–R3440.
- [31] Shan, B.; Ghimire, S.; Chang, Z. *J. Mod. Opt.* **2005**, *52*, 277–283.
- [32] Corkum, P.B.; Burnett, N.H.; Ivanov, M.Y. *Opt. Lett.* **1994**, *19*, 1870–1872.
- [33] Drescher, M.; Hentschel, M.; Kienberger, R.; Tempea, G.; Spielmann, C.; Reider, G.A.; Corkum, P.B.; Krausz, F. *Science* **2001**, *291*, 1923–1927.
- [34] Brabec, T.; Krausz, F. *Rev. Mod. Phys.* **2000**, *72*, 545–591.
- [35] Chipperfield, L.E.; Gaier, L.N.; Knight, P.L.; Marangos, J.P.; Tisch, J.W.G. *J. Mod. Opt.* **2005**, *52*, 243–260.
- [36] Haworth, C.A.; Chipperfield, L.E.; Robinson, J.S.; Knight, P.L.; Marangos, J.P.; Tisch, J.W.G. *Nat. Phys.* **2007**, *3*, 52–57.
- [37] Chipperfield, L.E.; Robinson, J.S.; Knight, P.L.; Marangos, J.P.; Tisch, J.W.G. *Laser Photonics Rev.* **2010**, *4*, 697–719.
- [38] Balcou, P.; Salières, P.; L’Huillier, A.; Lewenstein, M. *Phys. Rev. A* **1997**, *55*, 3204–3210.
- [39] Constant, E.; Garzella, D.; Breger, P.; Mével, E.; Dorrer, C.; Le Blanc, C.; Salin, F.; Agostini, P. *Phys. Rev. Lett.* **1999**, *82*, 1668–1671.
- [40] Rundquist, A.; Durfee, C.G.; Chang, Z.; Herne, C.; Backus, S.; Murnane, M.M.; Kapteyn, H.C. *Science* **1998**, *280*, 1412–1415.
- [41] Goulielmakis, E.; Yakovlev, V.S.; Cavalieri, A.L.; Uiberacker, M.; Pervak, V.; Apolonski, A.; Kienberger, R.; Kleineberg, U.; Krausz, F. *Science* **2007**, *317*, 769–775.
- [42] Salières, P.; L’Huillier, A.; Lewenstein, M. *Phys. Rev. Lett.* **1995**, *74*, 3776–3779.
- [43] Le Deroff, L.; Salières, P.; Carre, B. *Opt. Lett.* **1998**, *23*, 1544–1546.
- [44] Lee, D.G.; Park, J.J.; Sung, J.H.; Nam, C.H. *Opt. Lett.* **2003**, *28*, 480–482.
- [45] Salières, P.; L’Huillier, A.; Antoine, P.; Lewenstein, M. *Adv. At. Mol. Opt. Phys.* **1999**, *41*, 83–142.
- [46] Ditmire, T.; Gumbrell, E.T.; Smith, R.A.; Tisch, J.W.G.; Meyerhofer, D.D.; Hutchinson, M.H.R. *Phys. Rev. Lett.* **1996**, *77*, 4756–4759.
- [47] Itatani, J.; Quéré, F.; Yudin, G.L.; Ivanov, M.Y.u.; Krausz, F.; Corkum, P.B. *Phys. Rev. Lett.* **2002**, *88*, 173903.
- [48] Mairesse, Y.; Quéré, F. *Phys. Rev. A* **2005**, *71*, 011401(R).
- [49] Bradley, D.J.; Liddy, B.; Sleat, W.E. *Opt. Commun.* **1971**, *2*, 391–395.
- [50] Fieß, M.; Schultze, M.; Goulielmakis, E.; Dennhardt, B.; Gagnon, J.; Hofstetter, M.; Kienberger, R.; Krausz, F. *Rev. Sci. Instrum.* **2010**, *81*, 093103.
- [51] Sansone, G.; Benedetti, E.; Calegari, F.; Vozzi, C.; Avaldi, L.; Flammini, R.; Poletto, L.; Villoresi, R.; Altucci, C.; Velotta, R.; Stagira, S.; De Silvestri, S.; Nisoli, M. *Science* **2006**, *314*, 443–446.
- [52] Trebino, R.; DeLong, K.W.; Fittinghoff, D.N.; Sweetser, J.N.; Krumbügel, M.A.; Richman, B.A.; Kane, D.J. *Rev. Sci. Instrum.* **1997**, *68*, 3277–3295.
- [53] Kane, D.J. *J. Opt. Soc. Am. B* **2008**, *25*, 120–132.
- [54] Quéré, F.; Mairesse, Y.; Itatani, J. *J. Mod. Opt.* **2005**, *52*, 339–360.
- [55] Keller, U. *Nature* **2003**, *424*, 831–838.
- [56] Nisoli, M.; De Silvestri, S.; Svelto, O. *Appl. Phys. Lett.* **1996**, *68*, 2793–2795.
- [57] Nisoli, M.; De Silvestri, S.; Svelto, O.; Szpöcs, R.; Ferencz, K.; Spielmann, C.; Sartania, S.; Krausz, F. *Opt. Lett.* **1997**, *22*, 522–524.
- [58] Suda, A.; Hatayama, M.; Nagasaka, K.; Midorikawa, K. *Appl. Phys. Lett.* **2005**, *86*, 111116.
- [59] Robinson, J.S.; Haworth, C.A.; Teng, H.; Smith, R.A.; Marangos, J.P.; Tisch, J.W.G. *Appl. Phys. B* **2006**, *85*, 525–529.
- [60] Szpöcs, R.; Ferencz, K.; Spielmann, C.; Krausz, F. *Opt. Lett.* **1994**, *19*, 201–203.
- [61] Cavalieri, A.L.; Goulielmakis, E.; Horvath, B.; Helml, W.; Schultze, M.; Fieß, M.; Pervak, V.; Veisz, L.; Yakovlev, V.S.; Uiberacker, M.; Apolonski, A.; Krausz, F.; Kienberger, R. *New J. Phys.* **2007**, *9*, 242.
- [62] Park, J.; Lee, J.; Nam, C.H. *Opt. Lett.* **2009**, *34*, 2342–2344.
- [63] Witting, T.; Frank, F.; Arrell, C.A.; Okell, W.A.; Marangos, J.P.; Tisch, J.W.G. *Opt. Lett.* **2011**, *36*, 1680–1682.
- [64] Bohman, S.; Suda, A.; Kanai, T.; Yamaguchi, S.; Midorikawa, K. *Opt. Lett.* **2010**, *35*, 1887–1889.

- [65] Apolonski, A.; Poppe, A.; Tempea, G.; Spielmann, C.; Udem, T.; Holzwarth, R.; Hänsch, T.W.; Krausz, F. *Phys. Rev. Lett.* **2000**, *85*, 740–743.
- [66] Baltuška, A.; Fujii, T.; Kobayashi, T. *Phys. Rev. Lett.* **2002**, *88*, 133901.
- [67] Grebing, C.; Koke, S.; Manschwetus, B.; Steinmeyer, G. *Appl. Phys. B* **2009**, *95*, 81–84.
- [68] Goulielmakis, E.; Schultze, M.; Hofstetter, M.; Yakovlev, V.S.; Gagnon, J.; Uiberacker, M.; Aquila, A.L.; Gullikson, E.M.; Attwood, D.T.; Kienberger, R.; Krausz, F.; Kleineberg, U. *Science* **2008**, *320*, 1614–1617.
- [69] Abel, M.J.; Pfeifer, T.; Nagel, P.M.; Boutu, W.; Bell, M.J.; Steiner, C.P.; Neumark, D.M.; Leone, S.R. *Chem. Phys.* **2009**, *366*, 9–14.
- [70] Thomann, I.; Bahabad, A.; Liu, X.; Trebino, R.; Murnane, M.M.; Kapteyn, H.C. *Opt. Express* **2009**, *17*, 4611–4633.
- [71] Kim, K.T.; Kim, C.M.; Baik, M.-G.; Umesh, G.; Nam, C.H. *Phys. Rev. A* **2004**, *69*, 051805R.
- [72] Lan, P.; Lu, P.; Cao, W.; Wang, X.; Yang, G. *Phys. Rev. A* **2006**, *74*, 063821.
- [73] Ferrari, F.; Calegari, F.; Lucchini, M.; Vozzi, C.; Stagira, S.; Sansone, G.; Nisoli, M. *Nat. Photonics* **2010**, *4*, 875–879.
- [74] Sola, I.J.; Mével, E.; Elouga, L.; Constant, E.; Strelkov, V.; Poletto, L.; Villoresi, P.; Benedetti, E.; Caumes, J.-P.; Stagira, S.; Vozzi, C.; Sansone, G.; Nisoli, M. *Nat. Phys.* **2006**, *2*, 319–322.
- [75] Drescher, M.; Hentschel, M.; Kienberger, R.; Uiberacker, M.; Yakovlev, V.; Scrinzi, A.; Westerwalbesloh, T.; Kleineberg, U.; Heinzmann, U.; Krausz, F. *Nature* **2002**, *419*, 803–807.
- [76] Carlson, T.A.; Mullins, D.R.; Beall, C.E.; Yates, B.W.; Taylor, J.W.; Lindle, D.W.; Grimm, F.A. *Phys. Rev. A* **1988**, *39*, 1170–1185.
- [77] Uiberacker, M.; Uphues, T.; Schultze, M.; Verhoef, A.J.; Yakovlev, V.; Kling, M.F.; Rauschenberger, J.; Kabachnik, N.M.; Schröder, H.; Lezius, M.; Kompa, K.L.; Müller, H.-G.; Vrakking, M.J.J.; Hendel, S.; Kleineberg, U.; Heinzmann, U.; Drescher, M.; Krausz, F. *Nature* **2007**, *446*, 627–632.
- [78] Cavalieri, A.L.; Müller, N.; Uphues, T.; Yakovlev, V.S.; Baltuška, A.; Horvath, B.; Schmidt, B.; Blümel, L.; Holzwarth, R.; Hendel, S.; Drescher, M.; Kleineberg, U.; Echenique, P.M.; Kienberger, R.; Krausz, F.; Heinzmann, U. *Nature* **2007**, *449*, 1029–1032.
- [79] Schultze, M.; Fieß, M.; Karpowicz, N.; Gagnon, J.; Korbman, M.; Hofstetter, M.; Neppl, S.; Cavalieri, A.L.; Komninos, Y.; Mercouris, T.; Nicolaides, C.A.; Pazourek, R.; Nagele, S.; Feist, J.; Burgdörfer, J.; Azzeer, A.M.; Ernstorfer, R.; Kienberger, R.; Kleineberg, U.; Goulielmakis, E.; Krausz, F.; Yakovlev, V.S. *Science* **2010**, *328*, 1658–1662.
- [80] Kheifet, A.S.; Ivanov, I.A. *Phys. Rev. Lett.* **2011**, *105*, 233002.
- [81] Klünder, K.; Dahlström, J.M.; Gisselbrecht, M.; Fordell, T.; Swoboda, M.; Guénot, D.; Johnsson, P.; Caillat, J.; Mauritsson, J.; Maquet, A.; Taieb, R.; L’Huillier, A. *Phys. Rev. Lett.* **2011**, *106*, 143002.
- [82] Nabekawa, Y.; Shimizu, T.; Furukawa, Y.; Takahashi, E.J.; Midorikawa, K. *Phys. Rev. Lett.* **2009**, *102*, 213904.
- [83] Perry, M.D.; Crane, J.K. *Phys. Rev. A* **1993**, *48*, (R)4051–(R)4054.
- [84] Eichmann, H.; Egbert, A.; Nolte, S.; Momma, C.; Wellegehausen, B.; Becker, S.; Long, S.; McIver, J.K. *Phys. Rev. A* **1995**, *51*, (R)3414–(R)3417.
- [85] Kim, I.J.; Kim, C.M.; Kim, H.T.; Lee, G.H.; Lee, Y.S.; Park, J.Y.; Cho, D.J.; Nam, C.H. *Phys. Rev. Lett.* **2005**, *94*, 243901.
- [86] Chang, Z. *Phys. Rev. A* **2007**, *76*, 051403(R).
- [87] Oishi, Y.; Kaku, M.; Suda, A.; Kannari, F.; Midorikawa, K. *Opt. Express* **2006**, *7*, 7230–7237.
- [88] Mashiko, H.; Gilbertson, S.; Li, C.; Khan, S.D.; Shakya, M.M.; Moon, E.; Chang, Z. *Phys. Rev. Lett.* **2008**, *100*, 103906.
- [89] Gilbertson, S.; Mashiko, H.; Li, C.; Khan, S.D.; Shakya, M.M.; Moon, E.; Chang, Z. *Appl. Phys. Lett.* **2008**, *92*, 071109.
- [90] Feng, X.; Gilbertson, S.; Mashiko, H.; Wang, H.; Khan, S.D.; Chini, M.; Wu, Y.; Zhao, K.; Chang, Z. *Phys. Rev. Lett.* **2009**, *103*, 183901.
- [91] Constant, E.; Taranhukin, V.D.; Stolow, A.; Corkum, P.B. *Phys. Rev. A* **1997**, *56*, 3870–3878.
- [92] Altucci, C.; Delfin, C.h.; Roos, L.; Gaarde, M.B.; L’Huillier, A.; Mercer, I.; Starczewski, T.; Wahlström, C.-G. *Phys. Rev. A* **1998**, *58*, 3934–3941.
- [93] Chang, Z. *Phys. Rev. A* **2004**, *70*, 043802.
- [94] Gagnon, J.; Goulielmakis, E.; Yakovlev, V.S. *Appl. Phys. B: Lasers Opt.* **2008**, *92*, 25–32.
- [95] Chini, M.; Wang, H.; Khan, S.D.; Chen, S.; Chang, Z. *Appl. Phys. Lett.* **2009**, *94*, 161112.
- [96] Gilbertson, S.; Khan, S.D.; Wu, Y.; Chini, M.; Chang, Z. *Phys. Rev. Lett.* **2010**, *105*, 093902.
- [97] Tcherbakoff, O.; Mével, E.; Descamps, D.; Plumridge, J.; Constant, E. *Phys. Rev. A* **2003**, *68*, 043804.
- [98] Tzallas, P.; Skantzakis, E.; Kalpouzos, C.; Benis, E.P.; Tsakiris, G.D.; Charalambidis, D. *Nat. Phys.* **2007**, *3*, 846–850.
- [99] Altucci, C.; Esposito, R.; Tosa, V.; Velotta, R. *Opt. Lett.* **2008**, *33*, 2943–2945.
- [100] Tosa, V.; Kovacs, K.; Altucci, C.; Velotta, R. *Opt. Express* **2009**, *17*, 17700–17710.
- [101] Altucci, C.; Velotta, R.; Tosa, V.; Villoresi, P.; Frassetto, F.; Poletto, L.; Vozzi, C.; Calegari, F.; Negro, M.; De Silvestri, S.; Stagira, S. *Opt. Lett.* **2010**, *35*, 2798–2800.
- [102] Shin, H.J.; Lee, D.G.; Cha, Y.H.; Hong, K.H.; Nam, C.H. *Phys. Rev. Lett.* **1999**, *83*, 2544–2547.
- [103] Jullien, A.; Pfeifer, T.; Abel, M.J.; Nagel, P.M.; Bell, M.J.; Neumark, D.M.; Leone, S.R. *Appl. Phys. B* **2008**, *93*, 433–442.
- [104] Tosa, V.; Kim, T.K.; Nam, C.H. *Phys. Rev. A* **2009**, *79*, 043828.

- [105] Zamith, S.; Ni, Y.; Gürtler, A.; Noordam, L.D.; Muller, H.G.; Vrakking, M.J.J. *Opt. Lett.* **2004**, *29*, 2303–2305.
- [106] Pfeifer, T.; Gallmann, L.; Abel, M.J.; Neumark, D.M.; Leone, S.R. *Opt. Lett.* **2006**, *31*, 975–977.
- [107] Takahashi, E.J.; Lan, P.; Mücke, O.D.; Nabekawa, Y.; Midorikawa, K. *Phys. Rev. Lett.* **2010**, *104*, 233901.
- [108] Takahashi, E.J.; Lan, P.; Mücke, O.D.; Nabekawa, Y.; Midorikawa, K. *Phys. Rev. Lett.* **2010**, *105*, 049902.
- [109] Bandulet, H.-C.; Comtois, D.; Bisson, E.; Fleischer, A.; Pépin, H.; Kieffer, J.-C.; Corkum, P.B.; Villeneuve, D.M. *Phys. Rev. A* **2010**, *81*, 013803.
- [110] Pfeifer, T.; Gallmann, L.; Abel, M.J.; Nagel, P.M.; Neumark, D.M.; Leone, S.R. *Phys. Rev. Lett.* **2006**, *97*, 163901.
- [111] Fleischer, A.; Moiseyev, N. *Phys. Rev. A* **2006**, *74*, 053806.
- [112] Cao, W.; Lu, P.X.; Lan, P.F.; Wang, X.L.; Yang, G.A. *Phys. Rev. A* **2006**, *74*, 063821.
- [113] Bouhal, A.; Salières, P.; Breger, P.; Agostini, P.; Hamoniaux, G.; Mysyrowicz, A.; Antonetti, A.; Costantinescu, R.; Muller, H.G. *Phys. Rev. A* **1998**, *58*, 389–399.
- [114] Sekikawa, T.; Kosuge, A.; Kanai, T.; Watanabe, S. *Nature* **2004**, *432*, 605–608.
- [115] Pfeifer, T.; Jullien, A.; Abel, M.J.; Nagel, P.M.; Gallmann, L.; Neumark, D.M.; Leone, S.R. *Opt. Express* **2007**, *15*, 17120–17128.
- [116] Pfeifer, T.; Abel, M.J.; Nagel, P.M.; Boutu, W.; Bell, M.J.; Liu, Y.; Neumark, D.M.; Leone, S.R. *Opt. Lett.* **2009**, *34*, 1819–1821.
- [117] López-Martens, R.; Mauritsson, J.; Johnsson, P.; L’Huillier, A.; Tcherbakoff, O.; Zaïr, A.; Mével, E.; Constant, E. *Phys. Rev. A* **2004**, *69*, 053811.
- [118] Chang, Z. *Phys. Rev. A* **2005**, *71*, 023813.
- [119] Gaarde, M.B.; Tate, J.L.; Schafer, K.J. *J. Phys. B* **2008**, *41*, 132001.
- [120] Altucci, C.; Tosa, V.; Velotta, R. *Phys. Rev. A* **2007**, *75*, 061401(R).
- [121] Priori, E.; Cerullo, G.; Nisoli, M.; Stagira, S.; De Silvestri, S.; Villoresi, P.; Poletto, L.; Ceccherini, P.; Altucci, C.; Bruzzese, R.; de Lisio, C. *Phys. Rev. A* **2000**, *61*, 063801.
- [122] Milosevic, D.B.; Paulus, G.G.; Becker, W. *Phys. Rev. A* **2005**, *71*, 061404.
- [123] Gaarde, M.B.; Salin, F.; Constant, E.; Balcou, P.; Schafer, K.J.; Kulander, K.C.; L’Huillier, A. *Phys. Rev. Lett.* **1999**, *59*, 1367–1370.